



Review

Towards high strength cast Mg-RE based alloys: Phase diagrams and strengthening mechanisms

Janet M. Meier^a, Josh Caris^b, Alan A. Luo^{a,c,*}^aDepartment of Materials Science and Engineering, The Ohio State University, Columbus, OH 43210, USA^bTerves LLC, Euclid, OH 44117, USA^cDepartment of Integrated Systems Engineering, The Ohio State University, Columbus, OH 43210, USA

Received 23 December 2021; received in revised form 7 February 2022; accepted 31 March 2022

Available online 5 May 2022

Abstract

Mg-rare earth (RE) based systems provide several important commercial alloys and many alloy development opportunities for high strength applications, especially in aerospace and defense industries. The phase diagrams, microstructure, and strengthening mechanisms of these multicomponent systems are very complex and often not well understood in literature. We have calculated phase diagrams of important binary, ternary, and multicomponent RE-containing alloy systems, using CALPHAD (CALculation of PHase Diagrams). Based on these phase diagrams, this paper offers a critical overview on phase equilibria and strengthening mechanisms in these alloy systems, including precipitation, long period stacking order (LPSO), and other intermetallic phases. This review also summarized several promising Mg-RE based cast alloys in comparison with commercial WE54 and WE43 alloys; and explored new strategies for future alloy development for high strength applications. It is pointed out that the combination of precipitation and LPSO phases can lead to superior strength and ductility in Mg-RE based cast alloys. The precipitates and LPSO phases can form a complex three-dimensional network that effectively impedes dislocation motion on the basal and non-basal planes. The LPSO phases can also prevent the coarsening of precipitates when they interact, thus providing good thermal stability at elevated temperatures. Future research is needed to determine how the combination of these two types of phases can be used in alloy design and industrial scale applications.

© 2022 Chongqing University. Publishing services provided by Elsevier B.V. on behalf of KeAi Communications Co. Ltd.

This is an open access article under the CC BY-NC-ND license (<http://creativecommons.org/licenses/by-nc-nd/4.0/>)

Peer review under responsibility of Chongqing University

Keywords: Magnesium alloys; Phase diagrams; Precipitation strengthening; Long period stacking order (LPSO); Alloy development; CALPHAD.

1. Introduction

In the past two decades, the research and development of high strength magnesium (Mg) alloys has intensified with numerous publications including some review papers [1–14]. With low density (about 1/5 of iron and 2/3 of aluminum) and high specific strength, Mg alloys are promising to replace conventional alloys in many structural applications [2,13,15]. Mg alloys offer potential weight savings that can reduce fuel costs and emissions during shipping and use life [16,17] and lower

processing temperatures that can save energy during manufacturing and production compared to ferrous alloys [15].

The addition of rare earth (RE) elements to Mg can introduce many new phases and microstructure changes, resulting in several interesting strengthening mechanisms. Commercial alloys such as WE54 (Mg-5.3%Y-3.5%RE-0.5%Zr, wt%) and WE43 (Mg-4%Y-3%RE-0.5%Zr, wt%) are excellent sand cast alloys with attractive properties at room and elevated temperatures for the aerospace and defense industries [18]. In these alloys, RE is a mixture of 50% Nd and the remainder of other heavy rare earths such as Tb, Er, Dy and Gd. Both WE43 and WE54 alloys have significant age-hardening response due to the formation of Mg-RE β -series precipitates [10]. More recently, many experimental Mg-RE based alloys have been developed with long period stacking ordered (LPSO) phases

* Corresponding author at: Department of Materials Science and Engineering, The Ohio State University, Columbus, OH 43210, USA.

E-mail address: luo.445@osu.edu (A.A. Luo).

[9]. The strengthening mechanisms associated with RE additions can be classified into four major types: solid solution strengthening, grain refinement fine β -series precipitation, and the formation of long period stacking ordered (LPSO) phases [10,19,20]. Recent exploratory literature has evidenced a dramatic increase in the number of Mg-RE based alloys developed based on these strengthening mechanisms.

With the large amount of literature that has been published in the last two decades, this review aims to summarize what new understanding has been gained in the area of cast Mg-RE based alloys. Also, phase diagrams of many Mg-RE based systems are not readily available and the phase equilibria of these systems are very complex. The goals of this review are to (1) calculate phase diagrams and understand phase equilibria of several Mg-RE based alloy systems, (2) discuss the strengthening mechanisms from LPSO phases and β -series precipitate formation for improvements in mechanical properties, (3) summarize recent advancements in high strength cast Mg-RE alloys, and (4) explore new strategies for future alloy development for high strength applications.

In this article, several crystal structure acronyms are used: HCP for hexagonal close packed, FCC for face centered cubic, DHCP for double hexagonal close packed, and CBCO for c-axis base-centered orthorhombic.

2. Phase diagrams and phase equilibria

Phase diagrams are important road maps providing information on the conditions for phase formation or transformation in any material system caused by variation of temperature, composition, pressure or any other viable state variables [21]. Therefore, phase diagrams are often used for material design and process optimization as a starting point in the manipulation of alloy chemistry and processing variables to achieve desired microstructures. Until about the last decade of the 20th century, phase diagrams were determined primarily by meticulous and costly experimentation. Originated from the early work of Kaufman and Bernstein [22], the CALPHAD (CALculation of PHase Diagrams) approach [23,24], based on computational thermodynamics, has matured over the past few decades to calculate phase diagrams and predict phase equilibrium for complex multi-component systems. Commercial CALPHAD packages such as ThermoCalc [25], Pandat [26] and FactSage [27] are available for phase diagram calculations and phase equilibrium modeling. This section summarizes calculated phase diagrams, using Pandat software and PanMagnesium 2021 database, of important binary, ternary, and multi-component Mg-RE based alloy systems for high strength alloy development. Although phase diagrams are established for equilibrium conditions, they provide important understanding of alloy microstructure produced from industrial casting processes [24].

2.1. Mg-Nd system

Fig. 1 shows the calculated Mg-Nd phase diagram with three intermetallic phases, $Mg_{41}Nd_5$, Mg_3Nd , and $MgNd$,

stable at room temperature and one intermetallic (Mg_2Nd) formed at elevated temperatures as follows:

- 1) At 786 °C Liquid \rightarrow $MgNd$ + Nd(BCC, body-centered cubic)
- 2) At 759 °C Liquid \rightarrow Mg_3Nd + Mg_2Nd
- 3) At 758 °C Liquid \rightarrow Mg_2Nd + $MgNd$
- 4) At 662 °C Mg_2Nd \rightarrow Mg_3Nd + $MgNd$
- 5) At 559 °C Liquid + Mg_3Nd \rightarrow $Mg_{41}Nd_5$
- 6) At 548 °C Liquid \rightarrow $Mg_{41}Nd_5$ + Mg(HCP, hexagonal close packed)
- 7) At 511 °C Nd(BCC) \rightarrow $MgNd$ + Nd(HCP)

The maximum solubility of Nd is about 3.7 wt% at 548 °C and gradually decreases to essentially zero at about 300 °C. Despite the complex and controversial precipitation sequences reported in literature [10], the Mg-Nd has shown strong precipitation hardening with the equilibrium phase being $Mg_{41}Nd_5$.

2.2. Mg-Gd system

Fig. 2 is the calculated Mg-Gd phase diagram including four intermetallic phases stable at room temperature: Mg_5Gd , Mg_3Gd , Mg_2Gd and $MgGd$. Follows:

- 1) At 869 °C Liquid + Gd(BCC) \rightarrow $MgGd$
- 2) At 760 °C Liquid + $MgGd$ \rightarrow Mg_2Gd
- 3) At 684 °C Gd(BCC) \rightarrow Gd(HCP) + $MgGd$
- 4) At 655 °C Liquid + Mg_2Gd \rightarrow Mg_3Gd
- 5) At 609 °C Liquid + Mg_3Gd \rightarrow Mg_5Gd
- 6) At 548 °C Liquid \rightarrow Mg(HCP) + Mg_5Gd

The very high maximum solubility of Gd (23.7 wt% at the eutectic temperature of 548 °C), which dramatically decreases to essentially zero at about 150 °C, suggests an ideal system for precipitation hardening. However, it is often necessary to add 10 to 20 wt% Gd to have significant precipitation hardening response [10,19].

2.3. Mg-Y system

Fig. 3 shows the calculated Mg-Y phase diagram with three intermetallic phases stable at room temperature: $Mg_{24}Y_5$, Mg_2Y and MgY . These phases are formed as follows:

- 1) At 940 °C Liquid + Y(BCC) \rightarrow MgY
- 2) At 785 °C Liquid + MgY \rightarrow Mg_2Y
- 3) At 775 °C Y(BCC) \rightarrow MgY + Y(HCP)
- 4) At 616 °C Liquid + Mg_2Y \rightarrow $Mg_{24}Y_5$
- 5) At 574 °C Liquid \rightarrow Mg(HCP) + $Mg_{24}Y_5$

The maximum solubility of Y in Mg is 13.9 wt% at the eutectic temperature of 574 °C and gradually decreases to essentially zero at room temperature. The age-hardening response of binary Mg-Y alloys is remarkable when the Y concentration in the alloy is at or above 8 wt% and the aging treatment is carried out at a temperature close to 200 °C [10,19].

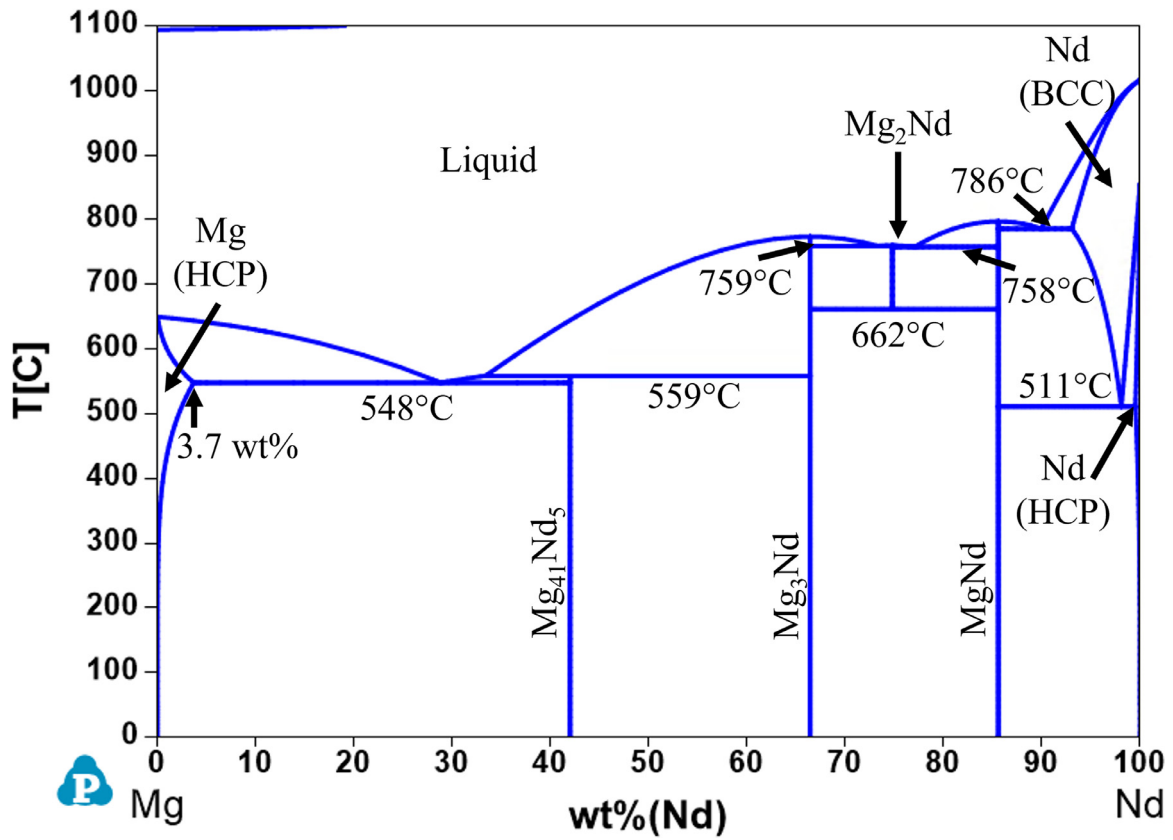


Fig. 1. Calculated Mg-Nd phase diagram.

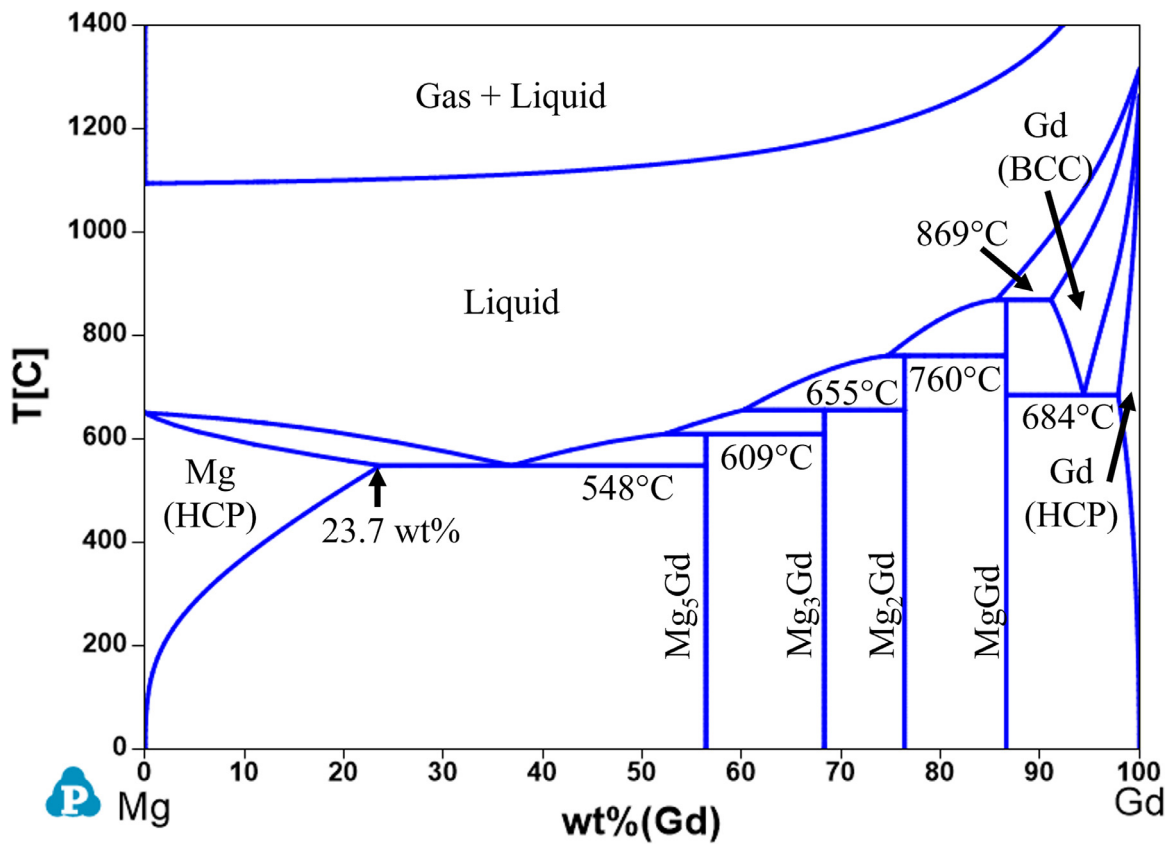


Fig. 2. Calculated Mg-Gd phase diagram.

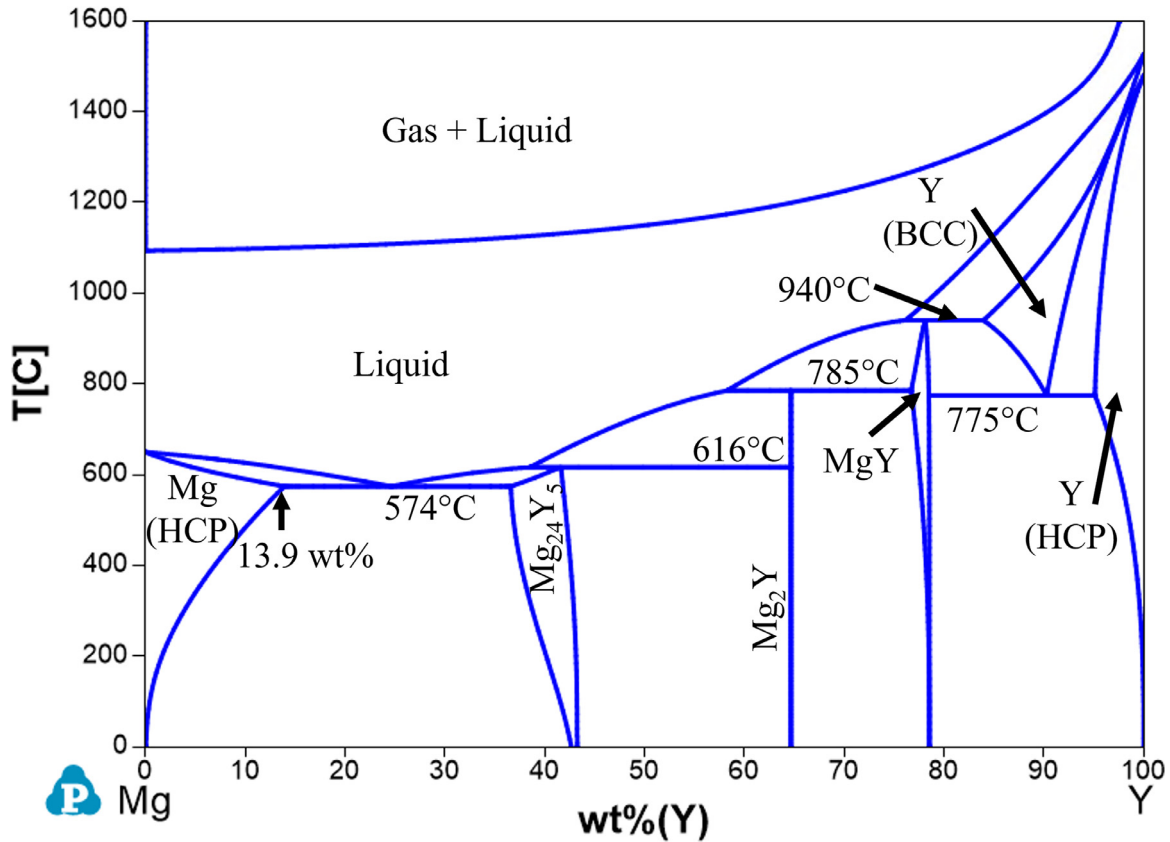


Fig. 3. Calculated Mg-Y phase diagram.

2.4. Other Mg-RE systems from misch metals

A common, lower cost source of RE elements are misch metals. These misch metals are a mix of different RE elements and often rich in Ce and La [20]. Although these elements are important in other alloying systems, they do not show the same precipitation hardening response in the binary systems as the Mg-Gd and Mg-Nd. This is due to the low solid solubilities of Ce and La in Mg [20]. The binary diagrams and phase equilibria are shown below.

Fig. 4 shows the calculated Mg-Ce phase diagram with three intermetallic phases stable at room temperature: Mg₁₂Ce, Mg₂₄Ce₅, Mg₃Ce and MgCe. These phases are formed as follows:

- 1) At 759 °C Liquid + Mg₃Ce → Mg₂Ce
- 2) At 710 °C Liquid → Mg₂Ce+ MgCe
- 3) At 677 °C Liquid → Mg₂Ce+ Ce(BCC)
- 4) At 625 °C Liquid + Mg₃Ce → Mg₄₁Ce₅
- 5) At 619 °C Mg₂Ce → MgCe + Mg₃Ce
- 6) At 617 °C Liquid + Mg₄₁Ce₅ → Mg₁₇Ce₂
- 7) At 611 °C Liquid + Mg₁₇Ce₂ → Mg₁₂Ce
- 8) At 609 °C Mg₁₇Ce₂ → Mg₄₁Ce₅ + Mg₁₂Ce
- 9) At 595 °C Liquid → Mg(HCP) + Mg₁₂Ce
- 10) At 472 °C Ce(BCC) → MgCe + Ce (FCC)
- 11) At 56 °C Ce (FCC) → MgCe + Ce(DHCP)

The maximum solubility of Ce in Mg is 0.8 wt% at the eutectic temperature of 595 °C and rapidly decreases to essentially zero at room temperature. The precipitates formed in the Mg-Ce binary system during age-hardening are similar to the Mg-Nd system, but the low solid solubility of Ce in Mg results in very limited strengthening [10,20].

Fig. 5 shows the calculated Mg-La phase diagram with three intermetallic phases stable at room temperature: Mg₁₂La, Mg₁₇La₂, Mg₃La and MgLa. These phases are formed as follows:

- 1) At 774 °C Liquid + Mg₃La → Mg₂La
- 2) At 743 °C Liquid → Mg₂La+ MgLa
- 3) At 727 °C Mg₂La → MgLa+ Mg₃La
- 4) At 715 °C Liquid → MgLa + La(BCC)
- 5) At 672 °C Liquid → Mg₁₇La₂ + Mg₃La
- 6) At 632 °C Liquid + Mg₄₁La₅ → Mg₁₇La
- 7) At 611 °C Liquid → Mg(HCP) + Mg₁₂La
- 8) At 546 °C La(BCC) → MgCe + La(FCC)
- 9) At 595 °C MgCe + La(FCC) → La(DHCP)

The maximum solubility of La in Mg is 0.23 wt% at the eutectic temperature of 613 °C and rapidly decreases to essentially zero at room temperature. There is almost no age-hardening response in the Mg-La system [20].

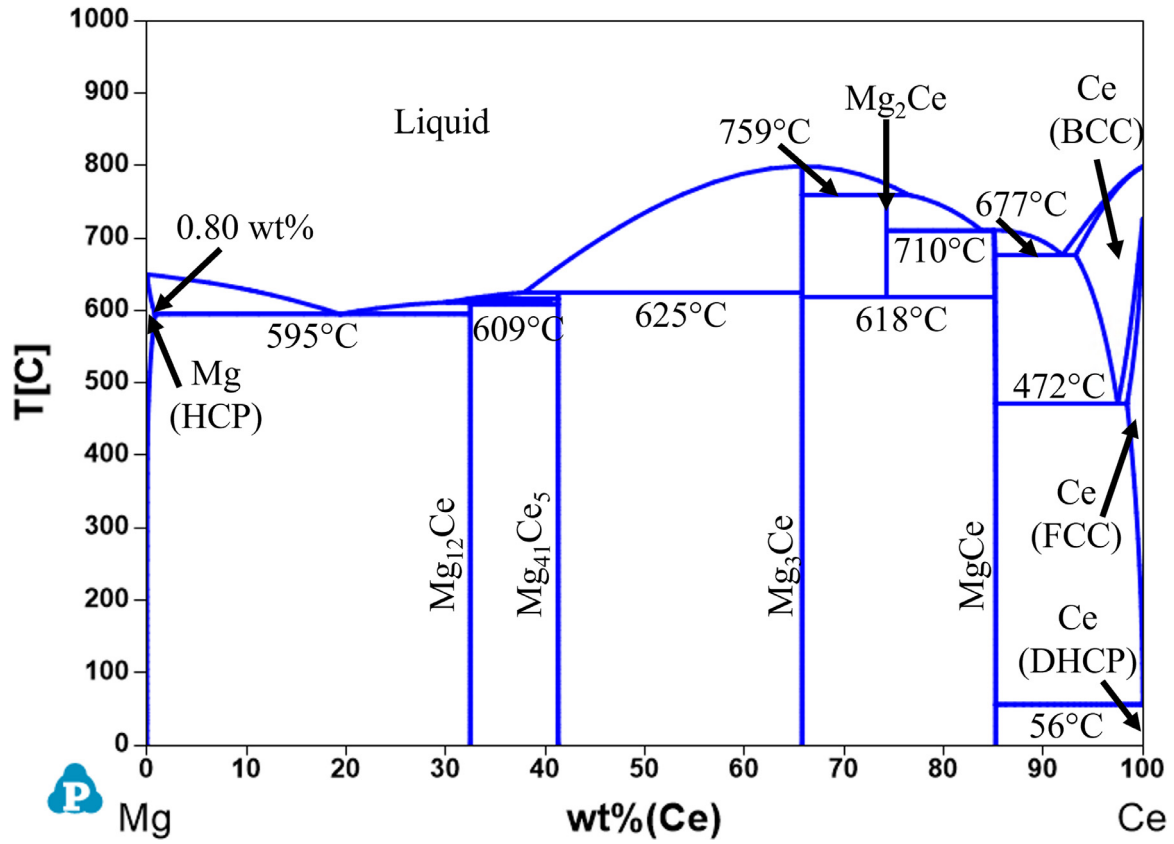


Fig. 4. Calculated Mg-Ce phase diagram.

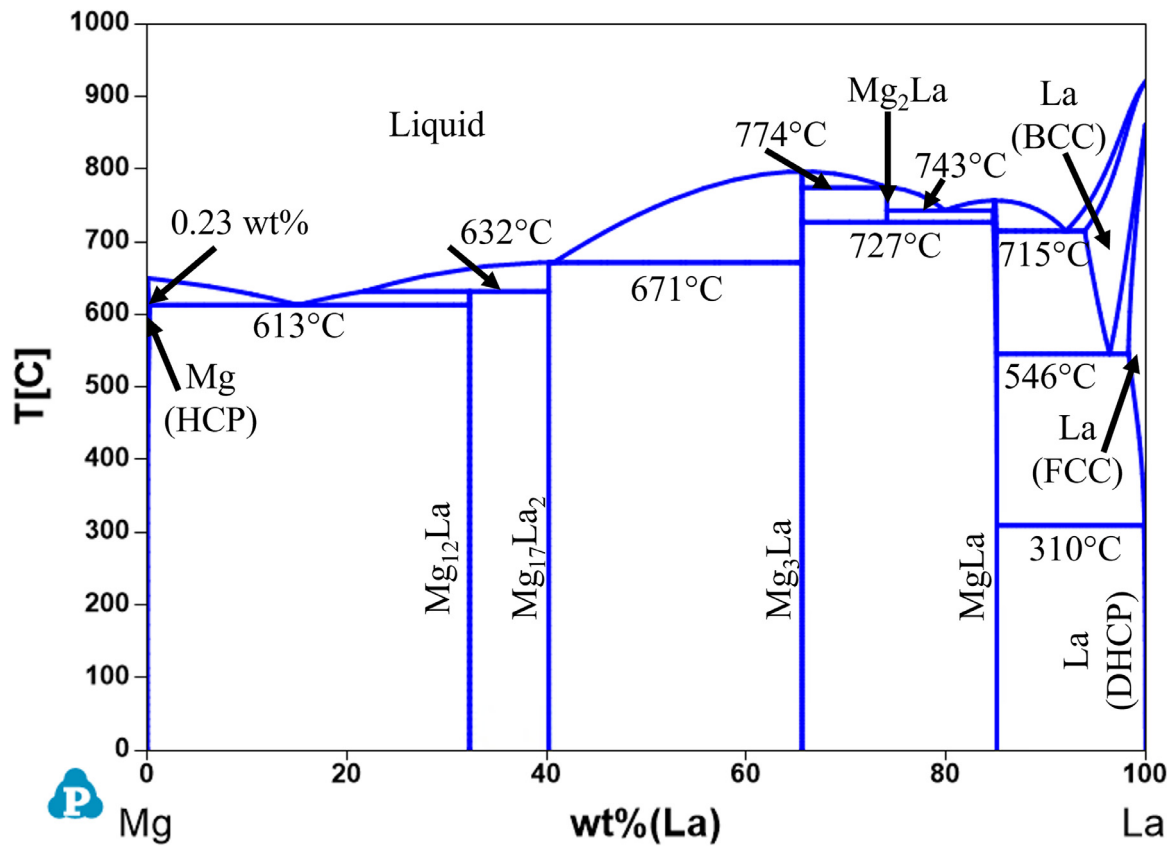


Fig. 5. Calculated Mg-La phase diagram.

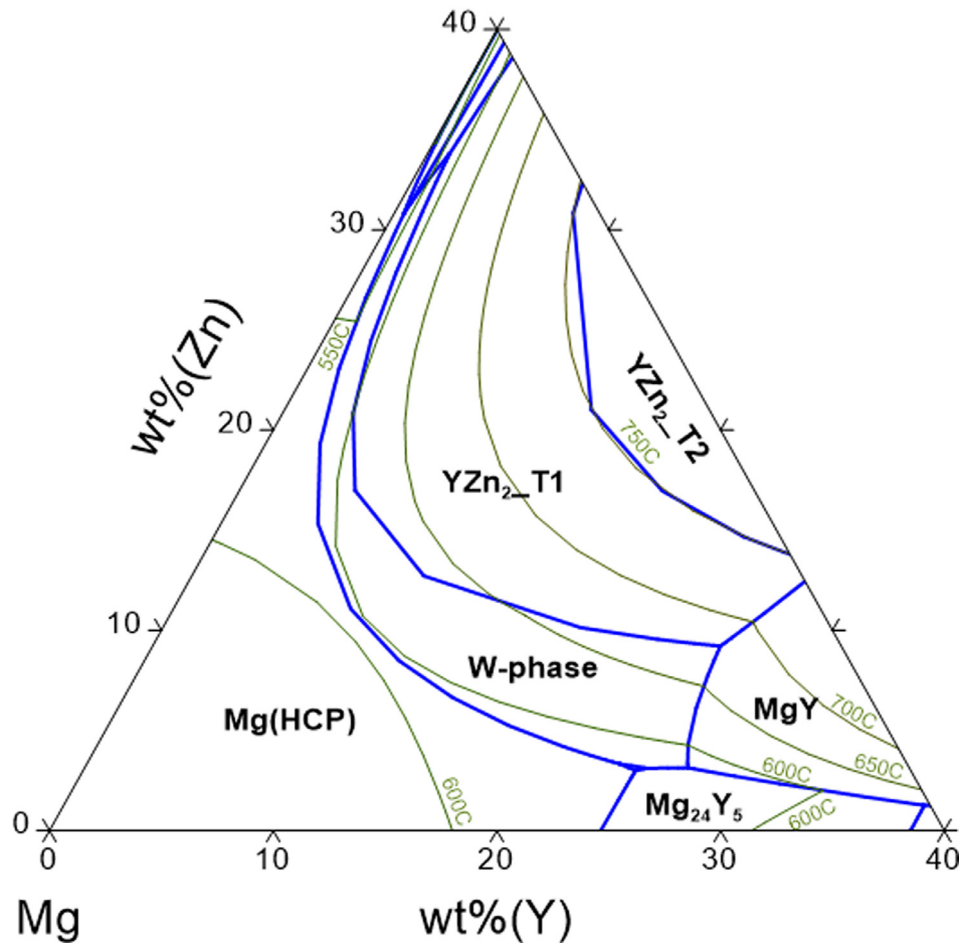


Fig. 6. Calculated ternary Mg-Y-Zn liquidus projection for up to 40 wt% Y and Zn. Blue lines indicate phase boundaries and green lines indicate the liquidous lines at different temperatures.

2.5. Mg-Y-Zn system

Fig. 6 shows the calculated Mg-Y-Zn liquidus projection for the Mg-rich corner. The invariant reactions for compositions where the Mg content is greater than or equal to 60 wt% are as follows:

- 1) At 675 °C Liquid + YZn_2 + MgY → W-phase ($\text{Mg}_3\text{Y}_2\text{Zn}_3$)
- 2) At 650 °C Liquid → Mg(HCP)
- 3) At 616 °C Liquid + Mg_2Y → Mg_{24}Y_5
- 4) At 612 °C Liquid + Mg_2Y → MgY + Mg_{24}Y_5
- 5) At 574.4 °C Liquid → Mg(HCP) + Mg_{24}Y_5
- 6) At 573.8 °C Liquid + MgY → W-phase + Mg_{24}Y_5
- 7) At 569 °C Liquid + $\text{YZn}_2\text{-T1}$ → Zn_5Y + W-phase
- 8) At 567 °C Liquid + Mg(HCP) + W-phase → LPSO_18R
- 9) At 566 °C Liquid + W-phase → Mg_{24}Y_5 + LPSO_18R
- 10) At 565 °C Liquid → Mg_{24}Y_5 + LPSO_18R + Mg(HCP)
- 11) At 526 °C Liquid + Zn_5Y → I-phase + W-phase

12) At 521 °C Liquid + W-phase → Mg(HCP) + I-phase (Mg_3YZn_6)

13) At 475 °C Liquid + I-phase → Mg(HCP) + $\text{Mg}_{28}\text{Y}_7\text{Zn}_{65}$

Fig. 7 shows isopleths for three different Y:Zn (at%) ratios to demonstrate how the phase stability changes throughout the ternary system. These plots are given in at% instead of wt% because the RE:Zn ratio in at% is most consistently used in literature. For a Y:Zn ratio of 0.5 (Fig. 7a), the predominate predicted solid phases are Mg(HCP) and W-phase. As the Y:Zn ratio is increased to 1 (Fig. 7b), three LPSO polytypes are predicted to form at lower temperatures: 14H, 18R, and 10H. The W-phase becomes less stable at lower temperatures as the Y:Zn ratio increases. At a Y:Zn ratio of 2 (Fig. 7c), the Y-rich β phase (Mg_{24}Y_5) becomes stable at lower temperatures and can coexist with the LPSO polytypes. In these calculated isopleths, LPSO 10H is predicted to be the most stable polytype. However, LPSO 14H is reported to be the most stable lower temperature polytype [5,9,28]. It is possible the transformation of LPSO 10H is very slow at the tempera-

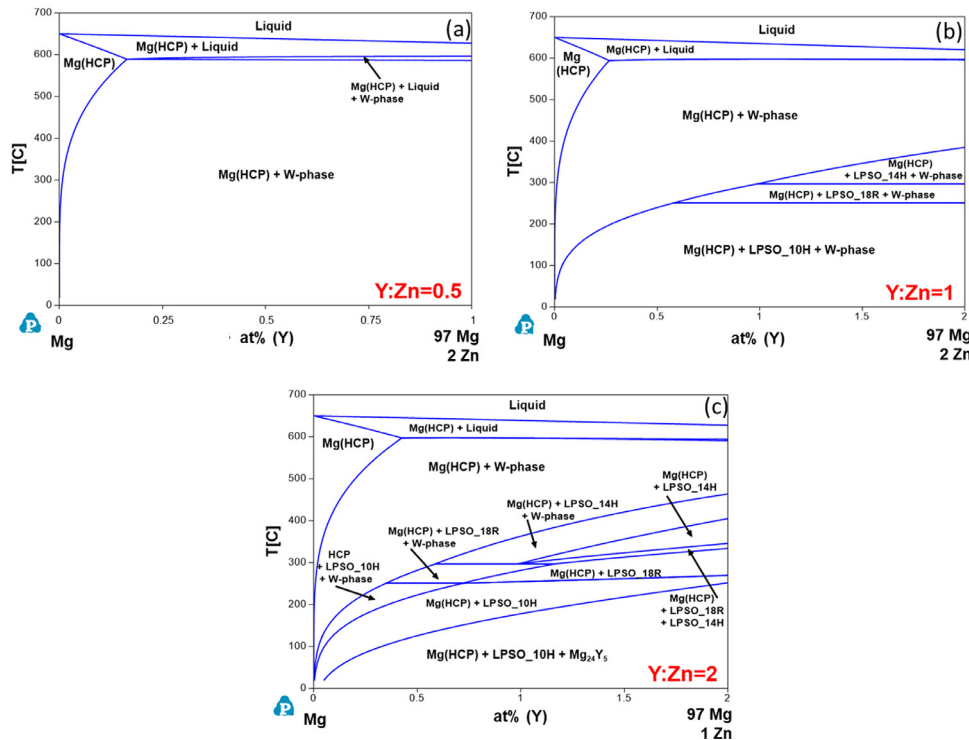


Fig. 7. Calculated isothermal sections of the Mg-Y-Zn ternary in the Mg-rich corner with Y:Zn ratios (at%) of (a) 0.5, (b) 1, and (c) 2.

tures when it is stable or the stability is overpredicted. More experimental investigation is needed to clarify the phase equilibria in this system.

2.6. Mg-Gd-Zn system

Fig. 8 shows the calculated Mg-Gd-Zn liquidus projection for the Mg-rich corner. The invariant reactions for compositions where the Mg content is greater than or equal to 60 wt% are as follows:

- 1) At 650 °C Liquid \rightarrow Mg(HCP)
- 2) At 589 °C Liquid + W-phase + $Mg_3Gd \rightarrow Mg_5Gd$
- 3) At 561 °C Liquid + $Mg_5Gd \rightarrow$ W-phase ($Mg_aGd_bZn_c$) + Mg(HCP)
- 4) At 548 °C Liquid $\rightarrow Mg_5Gd + Mg(HCP)$
- 5) At 506.5 °C Liquid + $Mg_3Gd_W \rightarrow Mg(HCP) + Gd_{20}Mg_{19}Zn_{81}F$

The composition and lattice parameter a W-phase (FCC structure, m3m) are affected by the composition of Mg-Zn-Gd alloys, especially by the Zn/Gd ratio of alloys [14]. Thus, it is presented as $Mg_aGd_bZn_c$ in this paper.

Fig. 9 shows the isopleth sections for various Gd:Zn ratios (at%). At a Gd:Zn ratio of 0.5 (Fig. 9a), Mg(HCP) and W-phase are the primary stable phases. An increase in Gd content to reach a Gd:Zn ratio of 1 (Fig. 9b) results in a decrease in stability of the W-phase. At high temperatures, the Gd-rich β phase (Mg_5Gd) is stable and LPSO 14H is stable at lower temperatures. At a Gd:Zn ratio equal to 2 (Fig. 9c),

the Gd-rich β phase becomes stable at both high and low temperatures.

2.7. Mg-Nd-Zn system

Fig. 10 shows the calculated Mg-Nd-Zn liquidus projection for the Mg-rich corner. The invariant reactions for compositions where the Mg content is greater than or equal to 60 wt% are as follows:

- 1) At 650 °C Liquid \rightarrow Mg(HCP)
- 2) At 558.5 °C Liquid + $Mg_3Nd \rightarrow Mg_{41}Nd_5$
- 3) At 548 °C Liquid $\rightarrow Mg(HCP) + Mg_{41}Nd_5$
- 4) At 650 °C Liquid + $Mg_{41}Nd_5 \rightarrow Mg_3Nd + Mg(HCP)$

Fig. 11 shows the isopleths for various Nd:Zn ratios in the Mg-Nd-Zn system. Unlike the previous two ternary systems, the W-phase and the LPSO polytypes are not formed in the Mg-Nd-Zn system. For a Nd:Zn ratio of 0.5 (Fig. 11a), four stable solid phases are predicted: Mg(HCP), Mg_3Nd , $Mg_{41}Nd_5$, and $Nd_8Mg_{50}Zn_{42}$. When the Nd:Zn ratio is increased to 1 (Fig. 11b), the stability of $Nd_8Mg_{50}Zn_{42}$ is reduced for intermediate temperatures. Further increase in Nd to a Nd:Zn ratio of 2 (Fig. 11c) results in the Nd-rich β phase ($Mg_{41}Gd_5$) becoming more stable for intermediate temperatures.

2.8. Mg-Gd-Y-Zn system

Fig. 12 shows the calculated Mg-Gd-Y ternary and three Mg-Gd-Y-xZn ($x = 0.5, 1, \text{ and } 1.5 \text{ wt\%}$) pseudo-ternary

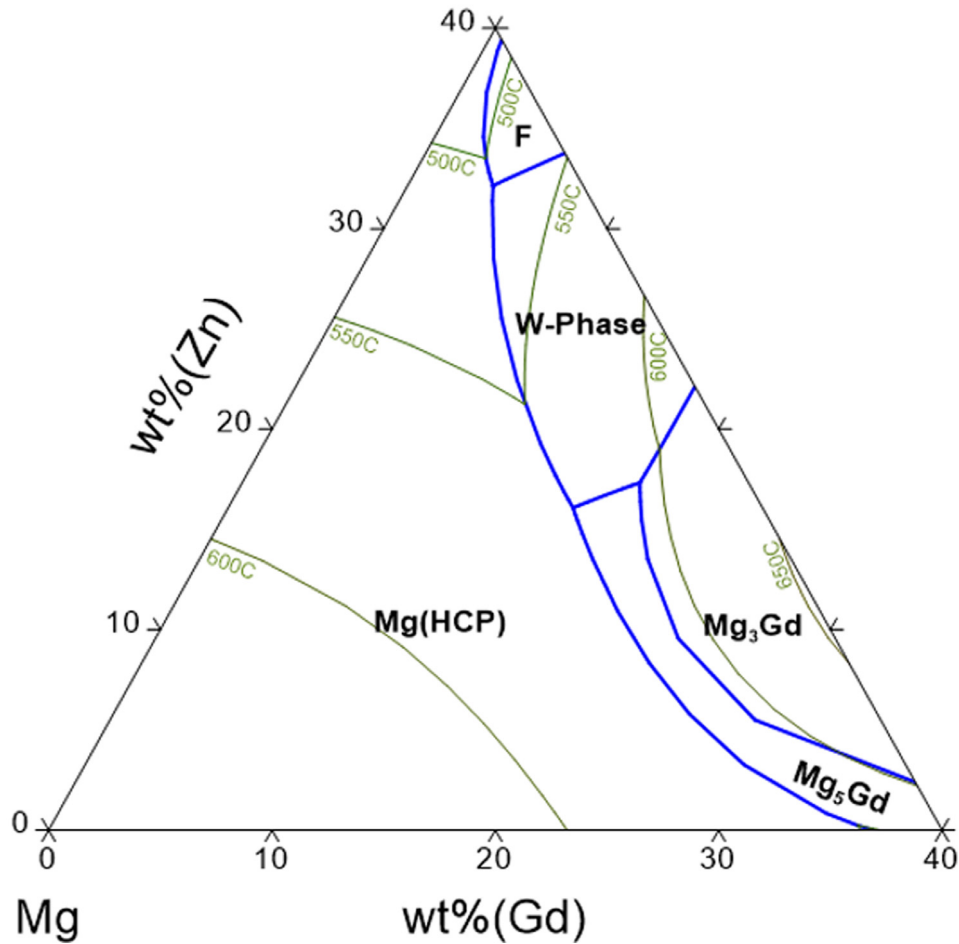


Fig. 8. Calculated ternary Mg-Gd-Zn liquidus projection for up to 40 wt% Gd and Zn. Blue lines indicate phase boundaries and green lines indicate the liquidus lines at different temperatures.

isotherms at 200 °C. The temperature of 200 °C was used for the calculations because it is a common T6 aging temperature in this alloy system. In the ternary system (Fig. 12a), the Mg-rich corner has three stable phases: Mg(HCP), Mg₅Gd, and Mg₂₄Y₅. When 0.5 wt% Zn is added to the Mg-Gd-Y system (Fig. 12b and c), LPSO 14H and the W-phase are formed and the single phase Mg(HCP) region shrinks significantly. An increase in Zn to 1.5 wt% (Fig. 12d) greatly increases the stability of the W-phase and decreases the stability of Mg₅Gd and Mg₂₄Y₅ at lower RE concentrations.

3. Precipitation strengthening

A comprehensive review of the precipitation hardening behavior in Mg alloys was given by Nie in 2012 [10]. Research on precipitation strengthening in Mg-RE alloys has heavily focused on the Mg-Gd and Mg-Nd alloy systems. This is due to the formation of very fine uniformly distributed β -series precipitates on the prismatic Mg planes [10,19,29,30]. These precipitates impede basal dislocations and result in improvements in mechanical properties [30]. This review will

focus on advancements in the understanding of β -series precipitation in the Mg-Gd and Mg-Nd systems, the effects of micro-alloying, and how the CALPHAD method can be used to predict precipitation behavior.

3.1. β -series precipitation

The β precipitation series in the Mg-Gd system has been consistently reported as follows [10]:

Super saturated solid solution(SSSS)

→ Guinier – Preston(G.P.)Zones

→ β'' (Mg₃Gd, HCP, D0₁₉) → β' (Mg₇Gd, CBCO)

→ β_1 (Mg₃Gd, FCC) → β (Mg₅Gd, FCC)

In the Mg-Nd system, the β precipitation series is slightly different [10]:

SSSS → G.P.Zones → β'' (Mg₃Nd, HCP, D0₁₉)

→ β' (Mg₇Nd, orthorhombic) → β_1 (Mg₃Nd, FCC)

→ β (Mg₄₁Nd₅, tetragonal)

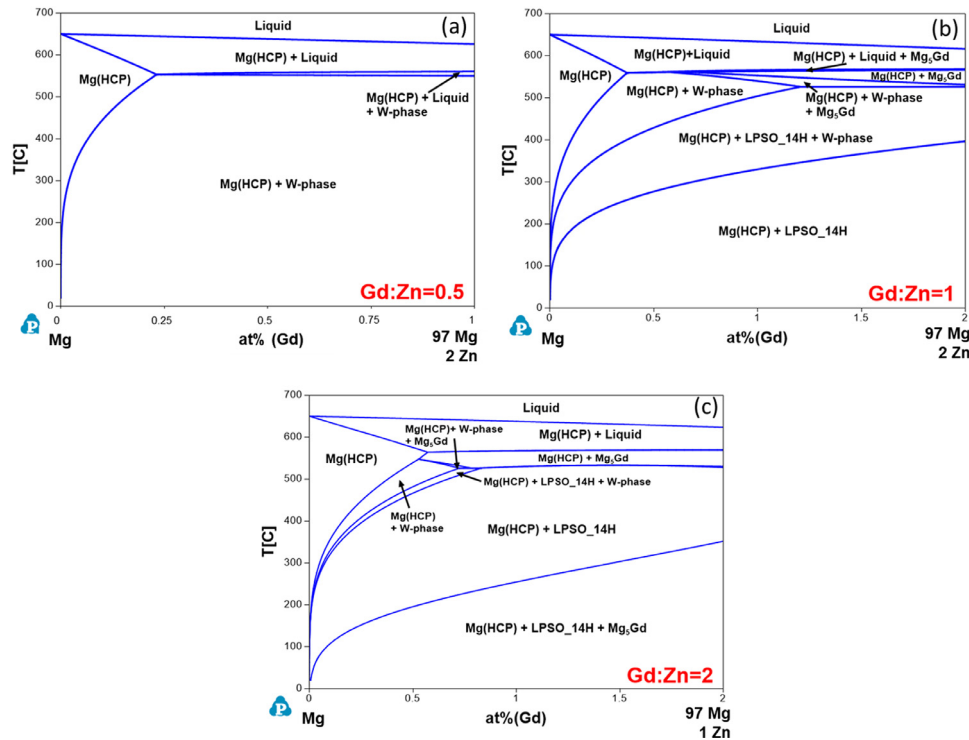


Fig. 9. Calculated isothermal sections of the Mg-Gd-Zn ternary in the Mg-rich corner with Gd:Zn ratios (at%) of (a) 0.5, (b) 1, and (c) 2.

Some variations have been reported with additional transition phases/structures [39], but for this review we will focus on these two generally accepted sequences. There is also some debate on the stability or existence of the β'' phase [29] that will not be discussed in full in this review.

The high maximum solubility of Gd (24 wt% or 4.6 at%) in Mg allows these systems to form the necessary SSSS needed for precipitation strengthening [31]. The drawback to precipitation strengthening in the Mg-Gd binary, from an economic standpoint, is that it requires a high concentration of Gd (~10 wt%) to produce significant mechanical property change [32]. Alternatively, in the Mg-Nd binary the maximum solid solubility of Nd (4 wt% or 2 at%) in Mg is significantly lower than that of Gd [31]. Thus, the necessary concentration to produce strengthening is also much lower for the Mg-Nd binary system [10].

During aging, the RE atoms segregate to form clusters and zig-zag monolayers that are comprised of RE rich columns (Fig. 13) [33]. These clusters and monolayers are classified as G.P. zones in most literature. The short-range ordering of RE atoms observed in the Mg-Gd and Mg-Nd systems, and the resulting G.P. zones, can form arrangements that resemble single layers of the β'' and β' structures [33]. In the case of β'' , the short-range ordering of RE atoms results in an arrangement of hexagonal prisms composed of six columns of RE atoms parallel to the $[0001]_{\alpha}$ direction and the prismatic plane of the hexagons is parallel to $\{2\bar{1}10\}_{\alpha}$ [33,34]. This arrangement, also referred to as super-hexagons, is consistent with the basal plane of the reported β'' $D0_{19}$ structure.

As previously mentioned, whether or not a β'' phase forms from these G.P. zones is currently under debate. The metastable β'' phase is generally reported to be Mg_3RE with a $D0_{19}$ structure [10]. The controversial nature of the β'' phase comes from conflicting structural descriptions, lack of experimental observation, and the similarities between the β'' phase description and other phase (i.e., G.P. zones and β'). For this review, the existence of the β'' will not be evaluated since the β' is the primary strengthening phase.

The β' phase has been consistently reported as Mg_7RE with a base centered orthorhombic structure ($a_{\beta'} = 2a_{Mg}$, $c_{\beta'} = c_{Mg}$) [10]. Interestingly, Mg_7Gd ($b_{\beta'} = 4\sqrt{3}a_{Mg}$) has a b lattice parameter twice that of Mg_7Nd ($b_{\beta'} = 2\sqrt{3}a_{Mg}$) [29]. A visualization of the two structures can be seen in Fig. 14. TEM analysis has shown that the β' phase grows as a thin plate along the $\{11\bar{2}0\}_{\alpha}$ prismatic Mg planes and are thus perpendicular to the Mg basal plane, as shown in Fig. 15 [30].

The strengthening effect of the β' phase is due to the disruption of basal slip and twinning in the HCP Mg lattice [10]. In HCP alloys, the basal plane is the most closely packed plane, and thus slip occurs more easily along the basal plane. As dislocations move along the basal planes, they encounter the dense triangular arrangement of the nanoscale β' and must either cut through or circumvent the precipitates [10,30]. Interestingly, in the Mg-Gd and Mg-Nd systems, the β' plates remain very thin in the $[1000]_{\alpha}$ direction and tend to have a large aspect ratio [10,29,30]. In the Mg-Nd system, β' has been reported to have a thickness of one unit cell in the $[1000]_{\alpha}$ direction, while β' in the Mg-Gd system may

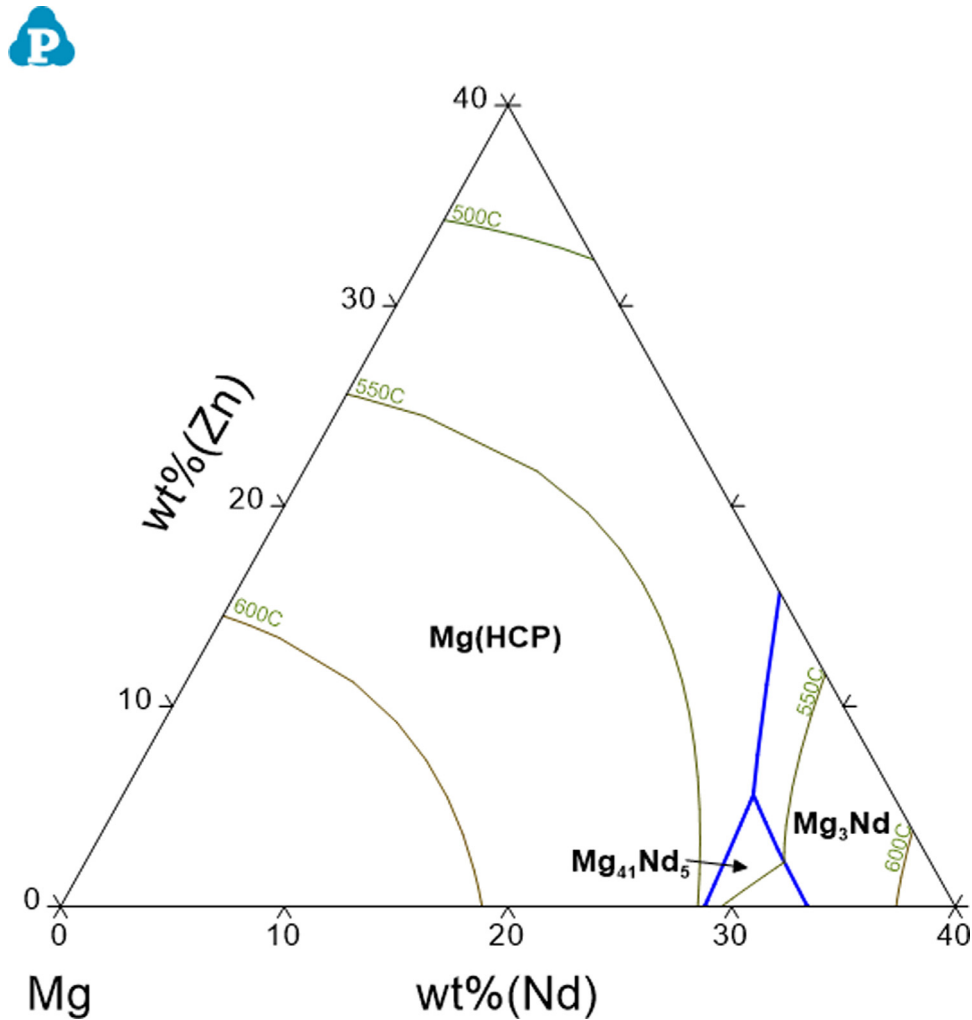


Fig. 10. Calculated ternary Mg-Nd-Zn liquidus projection for up to 40 wt% Nd and Zn. Blue lines indicate phase boundaries and green lines indicate the liquidous lines at different temperatures.

be a few unit cells in thickness [29]. In short, β' forms as very fine, thin precipitates with a high number density and strengthens the alloy by interrupting the primary slip system in the HCP Mg structure.

Issa et al. reported that the formation of β' is due to the instability of the Mg/ β'' interface, where β'' ($D0_{19}$, Mg_3RE) is the precursor phase to β' [29]. They used density function theory (DFT) first principles calculations to determine the basal and prismatic Mg/ β'' interfacial energies (Fig. 16). For the Mg-Nd system, there is a negative prismatic and a positive basal interfacial energy. This explains why the plates grow parallel to the prismatic plane but do not grow more than one unit cell thick parallel to the basal plate. The prismatic interfacial energy for the Mg-Gd system is negative, but the basal interfacial energy is also negative. Since the prismatic interfacial energy is still more negative, preferential growth will still occur parallel to the prismatic planes. The negative basal interfacial energy explains why the Gd-containing β' plates are thicker parallel to the basal plane than the Nd-containing

β' . These results indicate β' will form as thin plates with a large aspect ratio without the need of modification.

The β' phase is metastable, so continued aging results in transformations into other metastable and stable phases. It is generally reported that β' transforms into β_1 (Mg_3RE , FCC), which also provides some degree of strengthening to the alloy [10,35–37]. Since β' transforms into β_1 , it is still oriented along the prismatic planes and is found in the peak aged and over-aged conditions. The final stage is the equilibrium β phase, which is different in the two alloy systems. In the Mg-Gd system, β has a composition of Mg_5Gd , FCC structure and lattice parameter of $a = 2.2$ nm [10,36]. In the Mg-Nd system, β has a composition of $Mg_{41}Nd_5$, I4/m space group, and lattice parameters $a = 1.474$ nm and $c = 0.593$ nm [10,37]. Early literature identified the β as $Mg_{12}Nd$ but further study has determined $Mg_{12}Nd$ is another metastable β series phase and the equilibrium β is $Mg_{41}Nd_5$ [10]. The β for both systems can either form at the grain boundaries during solidification or as plates in the over-aged condition based on the β precipitation sequence. The β phase does not

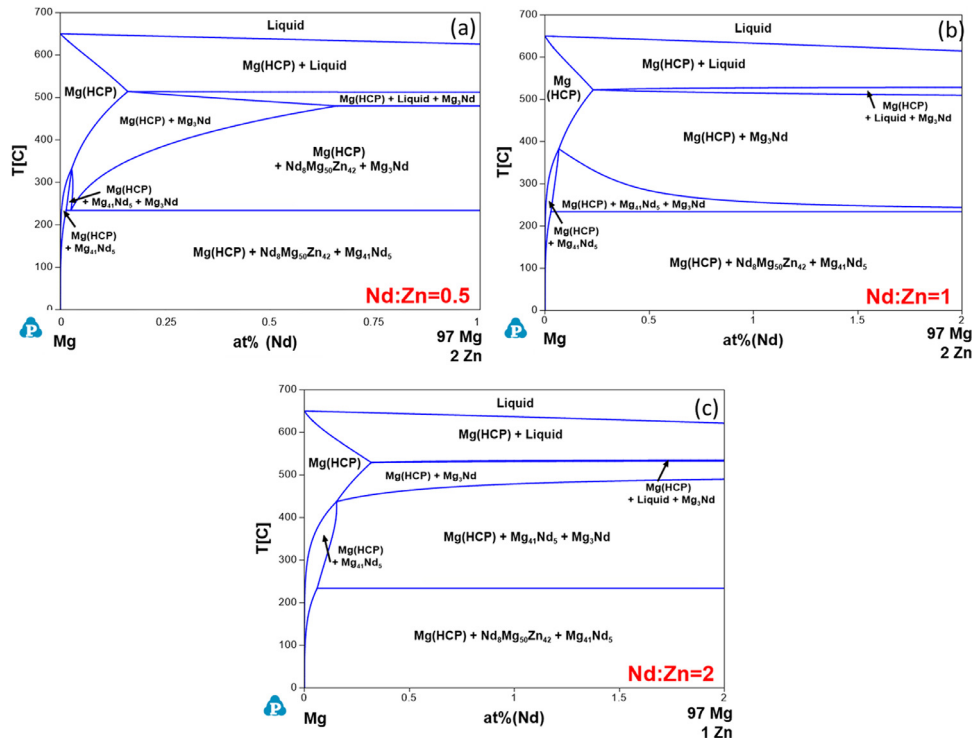


Fig. 11. Calculated isothermal sections of the Mg-Nd-Zn ternary in the Mg-rich corner with Nd:Zn ratios (at%) of (a) 0.5, (b) 1, and (c) 2.

provide the same strengthening as β' due to the growth of the precipitates, reduction of number density, and structural changes with aging [10].

3.2. Effects of micro-alloying elements

The β -series precipitation in the Mg-Gd and Mg-Nd systems can be significantly influenced by micro-alloying elements due to various thermodynamic and kinetic reasons. Although the current body of literature is small, this sub-section summarizes the recent research findings on the micro-alloying effects of Zn, Ca, and Ag on the Mg-Gd system and of Zn and Ca on the Mg-Nd system, which are critical to the development of high-strength Mg-RE based alloys based on precipitation strengthening.

3.2.1. Zn additions

3.2.1.1. Mg-Nd-Zn alloys. The effects of Zn on the Mg-Nd system were investigated by Zhou et al. in Mg-1Nd-1Ce-xZn-Zr ($x = 0, 0.2, 0.5, 1$, all wt%) alloys solution treated at 540 °C for 10 h and aged at 200 °C [38]. The peak-aged microstructure of the Zn-free composition contained two precipitates: disk-shaped precipitates located on the $\{11\bar{2}0\}_\alpha$ planes and point-like precipitates. The disk-like precipitates resembled imperfectly ordered β' and consisted of layers Nd-rich zig-zags and Nd-rich hexagons and were designated as β'' by the authors. The point-like precipitates were attributed to the segregation of Ce but need further investigation. The addition of Zn changed both size and density of β -series precipitates, and also introduced a plate-like basal phase. In the

0.2 wt% Zn alloy, the size of the reported β'' was reduced and the density increased. The fine basal precipitates were observed in a high density and identified as G.P. zones from the γ precipitation series. With an increase in Zn to 0.5 wt%, the number density of the basal precipitates increased, and basal precipitates became the dominate strengthening phase. The density of the β -series precipitates and point-like precipitates were greatly reduced. The density of precipitates was observed to decrease when 1 wt% Zn was added, and the β -series precipitates were no longer observed.

The time to reach the peak-aged condition increased with increasing Zn (8 to 16 h), but the peak-hardness only increases from ~ 58 HV (Zn-free) to ~ 60 HV (0.2 and 0.5 wt% Zn). In the peak-aged condition, the tensile yield strength (TYS) increased from 92 MPa to 136 MPa and the ultimate tensile strength (UTS) increased from 208 MPa to 237 MPa with increasing Zn from 0 to 0.5 wt%. The TYs (111 MPa) and UTS (210 MPa) both dropped with the addition of 1 wt% Zn. The elongation increased from 10% to 12.3% with an increase from 0 to 0.2 wt% Zn, dropped to 9% for the 0.5 wt% Zn alloy, and increased again to 11.7% for the 1 wt% Zn alloys. The increase in strength associated with the 0.2 wt% Zn alloy is attributed to refinement of the β -series precipitates and formation of fine basal precipitates. On the other hand, the strengthening in the 0.5 wt% Zn alloys is attributed to the increase in number density of basal precipitates since the β -series precipitates are no longer observed. The formation of the basal precipitates is dependent of a reduction of elastic strain due to co-segregation of RE and Zn atoms. This reduction in elastic strain, the reduction in RE

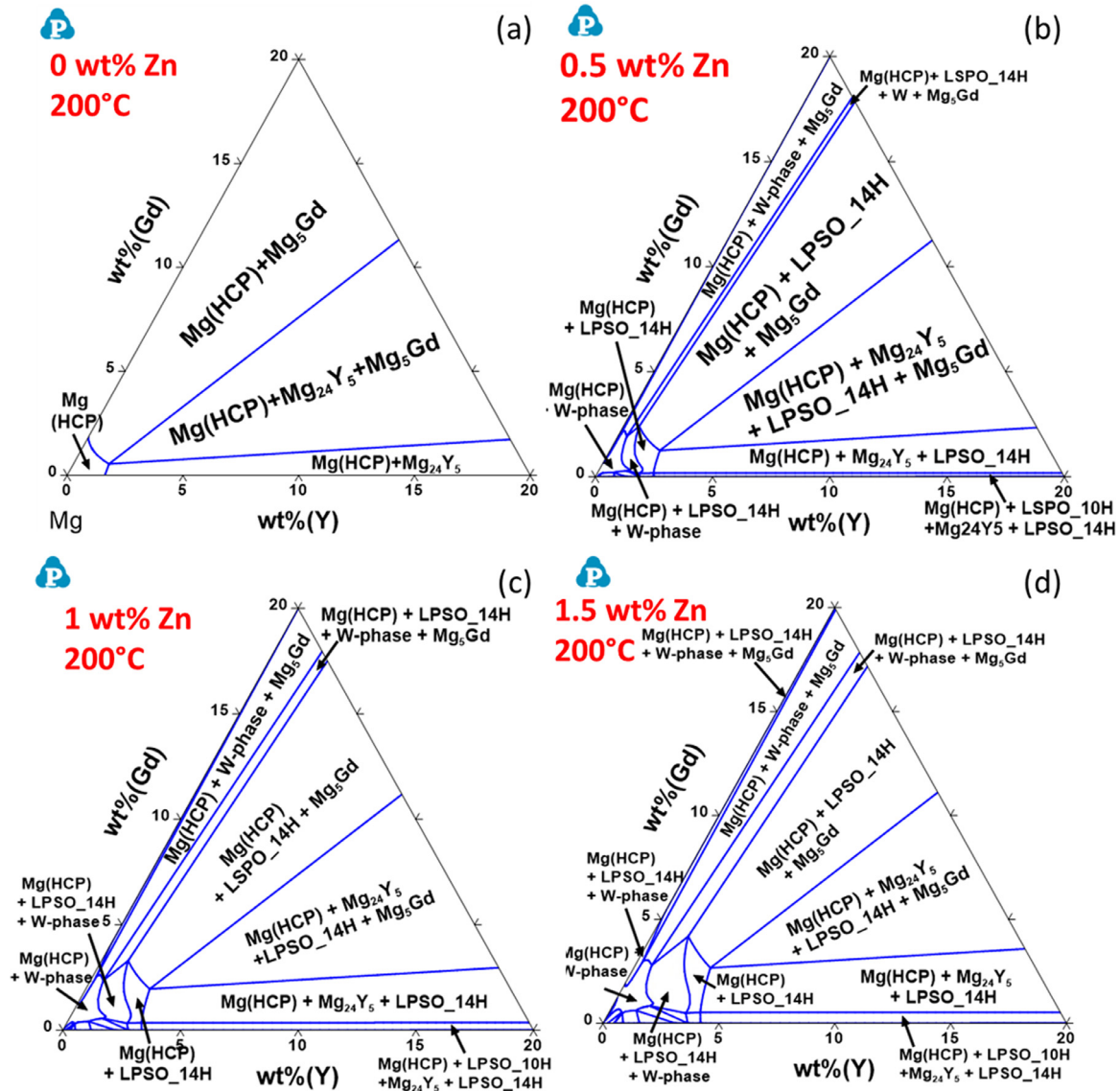


Fig. 12. Calculated isothermal sections of the (a) Mg-Gd-Y ternary and Mg-Gd-Y-xZn pseudo-ternary systems where x is (b) 0.5, (c) 1, and (d) 1.5 wt% Zn.

solubility caused by Zn, and the low solubility of Ce and Nd in Mg caused the precipitation hardening effect to be seen at low Zn additions. The higher solubility of Gd in Mg requires a larger Zn addition to see the same effect.

A study of the microstructural changes due to aging in a higher Nd-content (Mg-3Nd-0.2Zn, wt%) alloy was reported by Sanaty-Zadeh et al. [39]. Samples were homogenized at 540 °C for 5 h and aged in a 200 °C oil bath. The peak-aged condition was reached between 4 and 8 h. In the under-aged condition (2 h), four metastable phases were observed. The first phase type had a DO_{19} structure that was not fully developed, only exhibiting short range order, and was identified as G. P. I zones or as pre- β'' . The G.P. I zones were elongated plate like precipitates on the prismatic planes. The second phase type had a base centered orthorhombic structure and had a plate-like shape morphology (2 nm thick and 10–20 nm long) parallel to the prismatic planes that is consistent

with the β' phase. β' was observed to form independently as a single unit cell or transform from the G.P. I zones or β'' . The single unit cell version was designated as G.P. II zones. The third phase was an orthorhombic phase 5 nm long and 2 nm thick that was uniformly distributed throughout the matrix. Although similar to the β' phase, Sanaty-Zadeh et al. identified this as a new phase, β_2 . The fourth phase type formed on the prismatic planes and had a similar atomic arrangement to β_1 . This phase was not further identified. In the peak-aged condition (8 h), there was a uniform distribution of precipitates 10–30 nm long and 2–10 nm thick in the matrix that were identified as G.P. I zones, β' , β_2 , and β_1 . Of these phases, the β' and β_1 phases predominate. In this condition, β_1 was generally 10–30 nm long and 5–10 nm thick, but some larger precipitates 300–400 nm long and 10 nm thick were observed. In the over-aged condition (64 h), the β_1 phases is the predominate phase and the equilibrium β

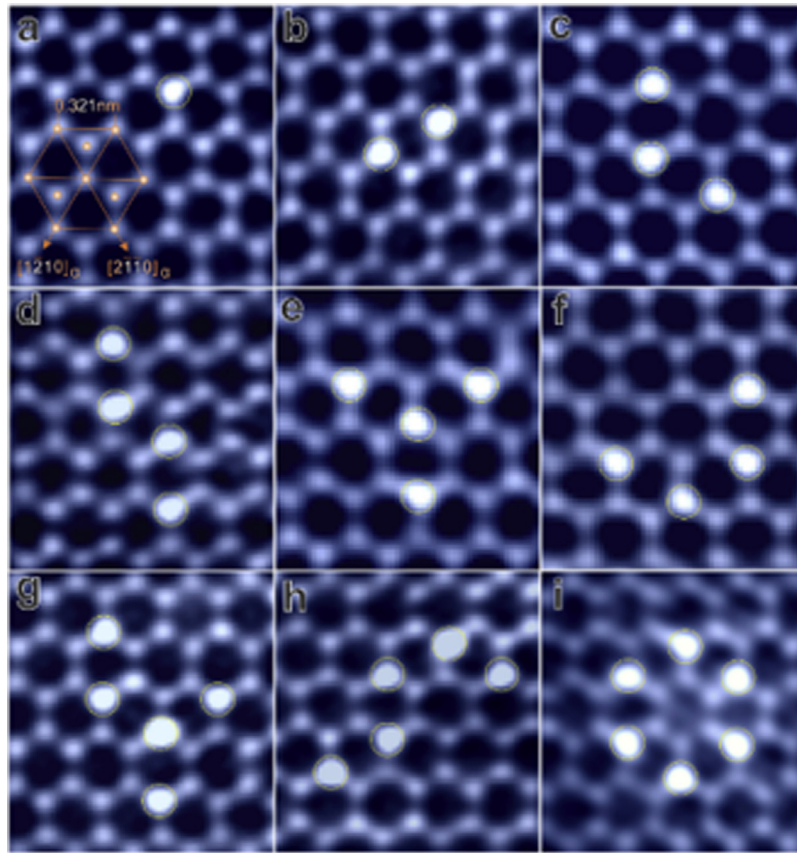


Fig. 13. Solute clusters observed using HAADF-STEM in an Mg-0.52 at% Nd alloy aged for 8 h at 200 °C. The electron beam was parallel to the $[0001]_{\alpha}$ direction [33].

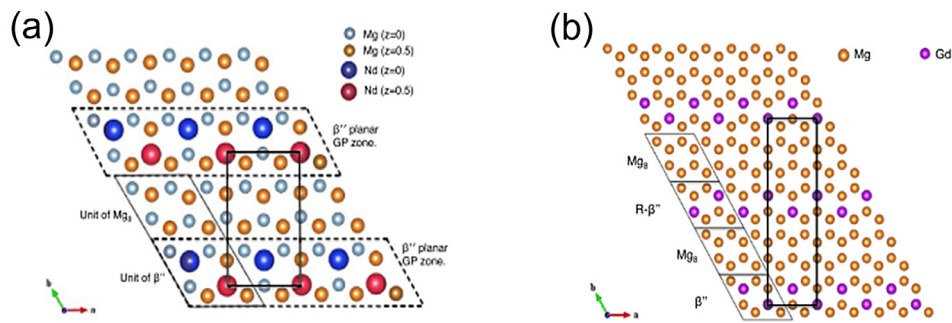


Fig. 14. Crystal structure of (a) Mg_7Nd and (b) Mg_7Gd [29].

phase is observed at the grain boundaries. In a few grains, an uneven distribution of needle-shaped basal precipitates similar to the γ' phase was also observed. The hardness of the alloy increased from ~ 52 HV in the solution treated condition to ~ 83 HV in the peak-aged condition.

Based on these findings, it can be seen that low levels of Zn additions refine and increase the number density of the β' . It also promotes the formation of basal precipitates. The combination of these two changes provides strengthening with increasing Zn additions until other phases start to form. Since the phase diagrams are for the equilibrium conditions, the metastable phases are not directly considered. Some assumptions can still be made based on these predictions. For

example, the possible fraction of β' can be determined based on the fraction of equilibrium β (Mg_5Gd or $Mg_{41}Nd_5$) and the stability of other RE containing phases. Fig. 17a shows the predicted pseudo-binary phase diagram for the Mg-2Nd-xZn (wt%) system. Here it can be seen that introducing Zn to the system promotes the formation of Mg_3Nd and the solubility of Zn in the matrix is less than 0.5 wt%. These predictions support the trend seen in the Mg-1Nd-1Ce-xZn-Zr (wt%) studied by Zhou et al. when the Zn content was increased from 0.5 to 1 wt% [38]. The increase in Zn promotes the formation of other Nd containing phases that cannot be removed with homogenization, thus introducing a competition for RE elements. This competition reduces the Nd available for the for-

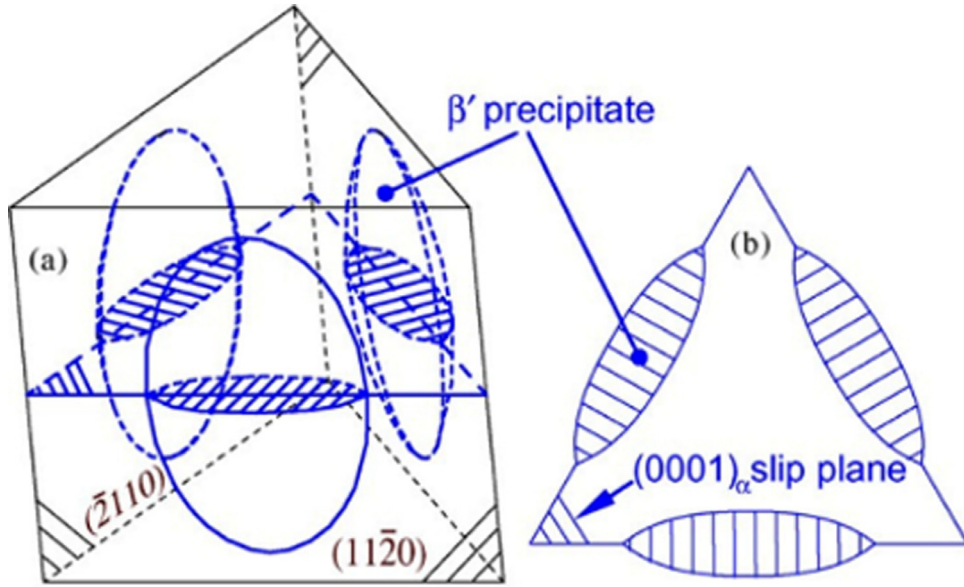


Fig. 15. Schematic of the (a) ideal β' precipitate orientation on the prismatic planes within the HCP crystal lattice and (b) the projection of the β' arrangement on the basal plane [30].

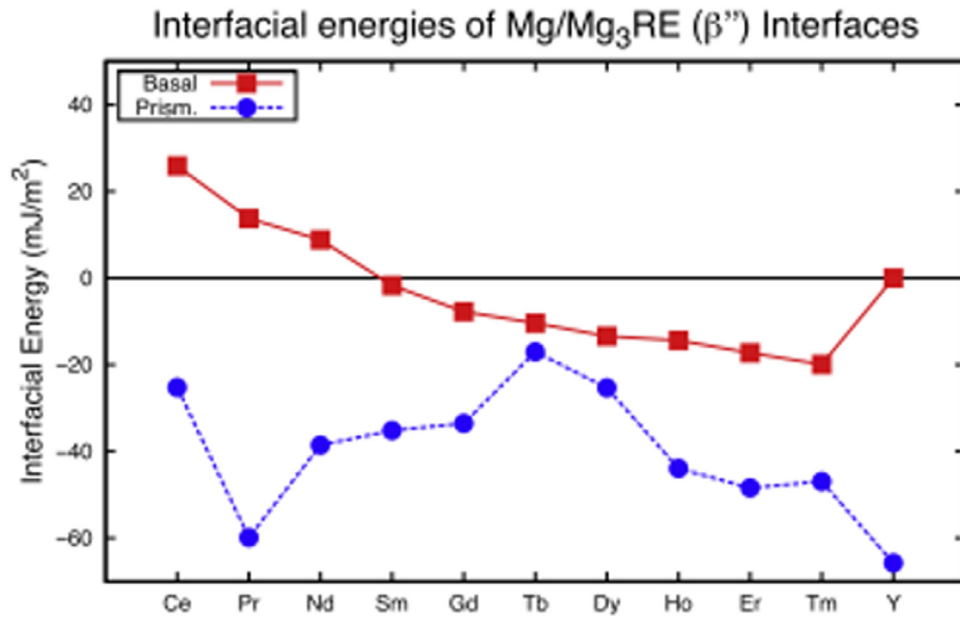


Fig. 16. Calculated Mg/ β'' interfacial energies at the basal (red, solid) and prismatic (blue, dashed) interfaces for eleven β -series forming RE [29].

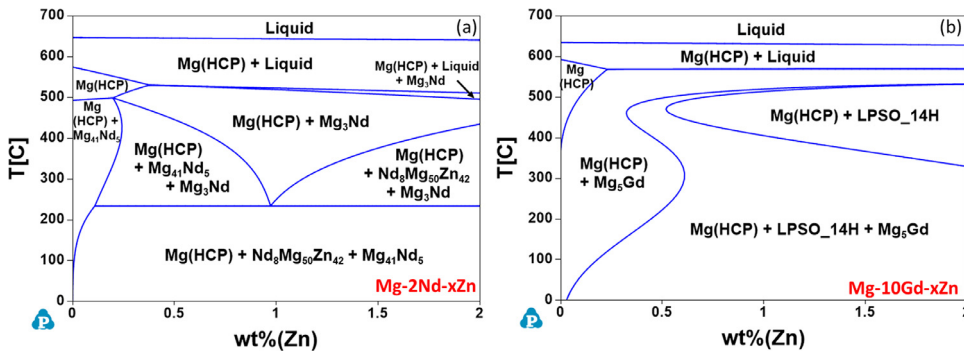


Fig. 17. Pseudo-binary diagrams of the (a) Mg-2Nd-xZn and (b) Mg-10Gd-xZn (wt%) systems.

mation of β' and thus the volume fraction is reduced. This indicates that the addition of Zn should be kept below the concentration where other non- β -series phases start to form. It should also be noted that $\text{Nd}_8\text{Mg}_{50}\text{Zn}_{42}$ is predicted to be stable in the temperature range used for aging. Depending on the kinetics for the formation of this phase, it may also precipitate during aging and should be considered.

3.2.1.2. Mg-Gd-Zn alloys. The effects of 1 wt% Zn on the Mg-Gd system were investigated by Gao and Nie on a Mg-6Gd-0.6Zr (wt%) alloy solution treated at 500 °C for 16 h and aged at 200 °C [40]. With the addition Zn, the peak-hardness increased from ~59 VHN after ~1200 h in the Zn-free alloy to 76 VHN after the same aging time. The 1 wt% Zn alloy exhibited a two-stage hardening response with an initial increase of hardness from 58 VHN in the as quenched condition to a plateau of ~64 VHN between 2 and 60 h. The microstructure of the Zn-free alloy contained small, uniformly distributed β' plates with a low number density. With the addition of 1 wt% Zn, the β' precipitates were completely replaced by plate-like basal precipitates. The basal plates were separated into two types based on size: ~70 nm in length and ~270 nm in length. The increased hardness is attributed to the formation of fine basal precipitates. The effects of larger Zn additions will be covered in more detail in a later section discussing LPSO-containing alloys.

These findings suggest that the basal precipitates may provide a greater strengthening effect than the β' in the Mg-Gd system. This is supported by previous works that indicate that the precipitation strengthening of β' is not as effective below 10 wt% Gd additions [10,32]. Fig. 17b shows the predicted pseudo-binary phase diagram for the Mg-10Gd-xZn (wt%) system. The Zn additions promote the formation of Mg_5Gd (the equilibrium phase in β -series precipitation) at higher temperatures and the formation of LPSO 14H as Zn increases. As with the Mg-Nd-Zn system, the single phase Mg(HCP) region is reduced as Zn increases. In the LPSO forming regions, there will be a competition for RE elements for phase formation. Thus, the Zn content must be kept low if the formation of β' or a single-phase region for homogenization is desired. Also, the γ -series basal precipitates can be thought of as precursors to the building blocks for the LPSO phase.

3.2.2. Ca additions

3.2.2.1. Mg-Nd-Ca alloys. Zheng et al. studied the age hardening response of a Mg-2Nd-1Y-0.1Zr-0.1Ca (wt%) alloy solution treated at 500 °C for 1 h [41]. After aging at 225 °C for 3 h, fine precipitates with a length <10 nm and a width <5 nm were observed sparsely distributed throughout the matrix. These precipitates took forms similar to the β' structure and grew parallel to the prismatic planes. At 42 h of aging (over-aged condition), the fine precipitates were replaced by coarser β_1 precipitates surrounded by precipitate-free zones (PFZ). β_1 precipitates remained parallel to $[10\bar{1}0]_\alpha$ and ~5 nm in width but were observed

to have grown to 35 to 50 nm in length. Between the as-solutionized and peak-aged condition (3 h), the hardness increased from 49 HV to 68 HV due to the fine β' -type precipitates. As more β_1 formed, the precipitates coarsened and the strengthening effect is weakened, thus the hardness dropped to 53 HV after 200 h of aging. EDS mapping showed the β_1 precipitates and coarse RE-containing phases along the grain boundaries were enriched with Ca. The authors proposed that the Ca is replacing the RE elements in these phases.

In an alloy with increased Ca (Mg-3Nd-1Ca, wt%), Sun et al. reported the microstructural changes after a solution treatment for 12 h at 520 °C and aging at 200 °C [42]. After 8 h of aging, β' and β_1 precipitates were observed in the matrix. The β' precipitates transformed into β_1 after 72 h of aging and the formation of “bubble-shaped” precipitates attached to the larger β_1 precipitates were observed. These “bubble-shaped” precipitates were 10 to 40 nm in size with a gray contrast. With continued aging for 240 h, these particles were no longer visible, indicating they are metastable, and only longer β_1 chains remained. Closer examination of the “bubble-shaped” precipitates using HAADF-STEM and SAED indicated they had a hexagonal structure ($a = 0.624$ nm and $c = 1.015$ nm). EDS analysis also indicated that Ca had segregated to the “bubble-shaped” precipitates while Nd was not detected. The bubble-shaped precipitates were identified as the Mg_2Ca C14 Laves phase. Interestingly, Nd was found to preferentially segregate to the shell of the Mg_2Ca particles. After 120 h, there was a different atomic arrangement observed for the “bubble-shaped” precipitates connecting the β_1 precipitates. The new arrangement closely resembles that of the γ'' basal plates with a thickness of approximately 5–20 nm along $[0001]_\alpha$. The authors defined a new γ''' phase that consisted of alternating γ'' (five atomic layers) and $(0001)_\alpha$ monolayers. The transformation of Mg_2Ca to γ''' basal plates is attributed to the incorporation of Nd into Mg_2Ca . The authors note γ''' is always observed alongside Mg_2Ca in these samples.

The addition of Ca to the Mg-Nd system promotes the formation of β_1 over β' . This is due to the lowering of the nucleation barrier and could result in a more refined distribution of precipitates in the later stages of aging. Similar to Zn, larger Ca additions result in the formation of basal precipitates as well as a Mg binary phase (Mg_2Ca in this case). There is also the indication that the Mg_2Ca may contribute to the formation of the basal precipitates. Fig. 18a shows the predicted pseudo-binary phase diagram for the Mg-2Nd-xCa system. The addition of Ca results in the formation of the Mg_2Ca C14 laves phase, which was observed by Sun et al. in their Mg-3Nd-1Ca (wt%) alloy. This phase does not compete for Nd to form and was observed to be in contact with the metastable γ''' basal precipitates. These predictions also support Mg_2Ca C14 laves not being observed in the Mg-2Nd-1Y-0.1Zr-0.1Ca (wt%) alloys studied by Zheng et al. As with the Zn additions, Ca additions result in the formation of other phases at high temperatures and thus reduces the composition range for the single-phase region needed for homogenization.

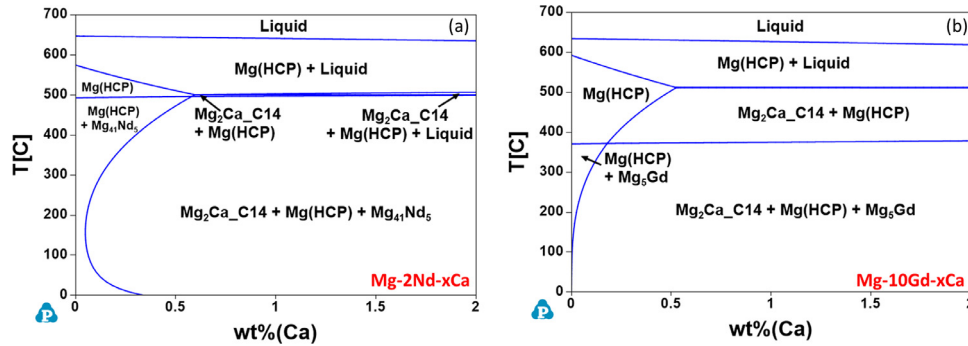


Fig. 18. Calculated pseudo-binary phase diagrams of the (a) Mg-2Nd-xCa and (b) Mg-10Gd-xCa (wt%) systems.

Unlike the Zn additions, the Mg_2Ca phase does not consume the Nd in the solution, so its formation likely does not have the same effect on β' precipitation.

3.2.2.2. Mg-Gd-Ca alloys. The effects of Ca additions on the aging response of a Mg-10Gd-xCa-0.5Zr ($x = 0, 0.3, 1.2$ wt%) alloy were studied by Shi et al. on samples aged at 200 °C after a 16 h solution treatment at 495 °C [43]. In the peak-aged condition, only β' precipitates were observed in the Ca-free alloy. On the other hand, the 0.3 and 1.2 wt% Ca alloys exhibited β' and long plate-like basal precipitates. The density of basal plates increased with increased Ca content. The basal plates were found to have an equal-atomic Ca and Gd content (in addition to Mg) while Ca segregation was not observed in the β' precipitates. The compressive yield strength (CYS), 213.0 MPa and 218.3 MPa, and ultimate compressive strength (UCS), 404.5 MPa and 393.2 MPa, in the peak-aged condition were similar between the Ca-free and 0.3 wt% Ca alloys, respectively. For the 1.2 wt% Ca alloy, the CYS and UCS increased to 253.2 MPa and 450.5 MPa, respectively. The peak-aged TYS increased from 181.0 MPa to 217.5 MPa with the addition of 1.2 wt% Ca. On the other hand, the UTS increased from 274.0 MPa to 304.8 MPa with the addition of 0.3 wt% Ca, but decreased back to 282.7 MPa with the addition of 1.2 wt% Ca. The authors state that the strengthening effect of the basal precipitates is negligible, but do not account for the increase in mechanical properties with the addition of Ca. It is possible the Ca is either increasing the number density of β' precipitates or the strengthening effect of the basal precipitates needs to be explored further.

The Ca additions to the Mg-Gd system were also investigated by Chen et al. using a base Mg-15Gd-0.5Zr (wt%) alloy [44]. In their work, the precipitate microstructure was characterized for additions of 0 and 0.6 wt% Ca after a solution treatment at 505 °C for 24 h and aging at 250 °C. After 1 h of aging the formation of a high number density of evenly distributed G.P. zones and β were observed in the Ca-free and 0.6 wt% Ca samples. In the 0.6 wt% Ca alloy, an additional Ca-rich and Gd-rich blocky phase that was 50–150 nm long and 45 nm thick was observed on the basal plane. In the peak-aged condition, both alloys primarily had β' precipitates,

but the 0.6wt% alloy also exhibited basal precipitates. The precipitates were 200 nm–1 μm in length and 14 nm thick and were enriched with Ca and Gd. Atomic-resolution HAADF-STEM and fast Fourier transform analysis indicates this phase was Mg_2Ca . After 32 h, the Ca-free alloy showed a limited change in precipitation, but in the 0.6 wt% Ca sample coarse β precipitates were observed. The β precipitates were 100–400 nm long and 20–50 nm thick and were enriched with Ca. In addition to the formation of β , the number density and size of the basal precipitates increased. Further aging for 64 h of the Ca-free alloy produced the formation of coarser β and β_1 precipitates. In the 0.6 wt% Ca alloy, the number density and size of β precipitates increase and fine β_1 precipitates were observed. EDS mapping indicated minor segregation of Ca to the β_1 precipitates. The Ca free alloy had an as-quenched hardness of 74 HV and reached a peak hardness of 107 HV after 8 h. The 0.6 wt% Ca sample increase from an as quenched hardness of 86 HV to ~ 120 HV at peak hardness after 4 h aging. In addition to the faster and greater age hardening response, the 0.6 wt% Ca sample also exhibited faster over-aging. The formation of the basal precipitates contributed to the increase in hardness, but the segregation of Ca to the β_1 and β series precipitates contributed to the acceleration of over-aging.

In a low Gd and higher Ca content alloy (Mg-3Gd-2Ca, wt%), Mo et al. investigated the age hardening response at 180 °C after a 16 h solution treatment at 510 °C [45]. A peak hardness of 66 HV was achieved after 32 h, an increase from ~ 50 HV in the as-quenched condition. In the peak-aged condition, there was an increase in CYS from 95 MPa to 150 MPa and UCS of 236 to 272 MPa from T4 condition. The increase in mechanical properties is attributed to the formation of three types of precipitates observed in the Mg matrix. The first type of precipitate was identified as Mg_2Ca and was reported to heterogeneously nucleate on pre-existing dislocations. Mg_2Ca exhibited a blocky morphology and the authors reported that it likely formed on the $\{11\bar{2}0\}_\alpha$ planes. The second type of precipitate, with a rod-shaped morphology on the prismatic planes, was identified as the β phase. In this alloy, the β phase was found in both the T4 and T6 conditions. The final precipitate type was sparsely distributed

basal plates with a large aspect ratio. The basal precipitates had an almost equal-atomic content of Ca and Gd (in addition to the Mg) and were fully coherent with the Mg matrix. The strengthening effect in the peak-aged condition is attributed to the Mg₂Ca and β precipitates, not the basal precipitates due to the low phase fraction. The authors propose the presence of β instead of the metastable β' may be due to the low Gd content and the lowering of the β nucleation barrier due to Ca additions.

In the Mg-Gd system, Ca additions result in the refinement of β' and the formation of basal precipitates. This can increase the alloy strength, but segregation of Ca to β_1 and β can accelerate over aging as the Ca concentration increases. Thus, the Ca additions may need to be kept low to prevent over-aging. Fig. 18b shows the predicted pseudo-binary phase diagram for the Mg-10Gd-xCa system. It can be seen that Ca additions promote the stability of Mg₅Gd at higher temperatures. As with the Nd-containing system, Mg₂Ca becomes stable with Ca additions. In the work by Mo et al., strengthening was partially attributed to Mg₂Ca. This could offer another strengthening mechanism that does not compete with the β -series precipitation like the LPSO does in the Zn-containing system.

3.2.3. Ag additions

3.2.3.1. Mg-Gd-Ag alloys. The effects of 2 wt% Ag on the Mg-Gd system were investigated by Gao and Nie on a Mg-6Gd-0.6Zr (wt%) alloy solution treated at 500 °C for 16 h and aged at 200 °C [40]. The addition of Ag resulted in an acceleration in age-hardening response. The peak aged condition was reached in 50 h instead of 1200 h for the Ag-free alloy and the peak hardness increased from 59 VHN to 80 VHN. The microstructure of the Ag-free alloy contained small, uniformly distributed β' plates with a low number density. The addition of 2 wt% Ag resulted in the formation of a high number density of basal plates \sim 25 nm in length. β' was not reported in the 2 wt% Ag alloy. The increase in hardness is attributed to the formation of fine basal precipitates.

In an alloy with a higher Gd content (Mg-3.4Gd-0.1Zr at% or Mg-18.7Gd-0.3Zr wt%), Yamada et al. examined the effects of Ag additions from 0.25 to 0.75 at% (0.9 to 2.7 wt%) after solution treatment and aging at 200 °C [46]. In the peak-aged condition, the 0.25 at% Ag (0.9 wt%) and 0.5 at% Ag (1.8 wt%) samples had hardness values of \sim 136 HV and \sim 137 HV, respectively. An increase to 0.75 at% Ag (2.7 wt%) resulted in an increased time to reach the peak-aged condition and the peak-hardness was reduced to \sim 125 HV. The reduction in hardness for the 0.75 at% Ag composition is attributed to the formation of a Mg-Gd-Ag phase that is not eliminated during solution treatment and thus less Ag is in the solid solution. The tensile properties for the peak-aged condition showed a similar trend to the hardness results. With an increase from 0.25 to 0.5 at% Ag the TYS was increased from 272 MPa to 293 MPa, the UTS increased from 338 MPa to 414 MPa, and the elongation increased from 1.4% to 2.2%. With a further increase to 0.75 at% Ag, the TYS was 292 MPa, the UTS dropped to 358 MPa, and the elongation

dropped to 1.5%. The increase in Ag content from 0.25 to 0.5 at% corresponds to an increase in the number density and thickness of the basal plates. The structure of the basal precipitates is different for the 0.75 at% Ag composition and closely resembles the ternary Mg₁₂Gd₂Ag phase. Although β' precipitates were observed, the increased strengthening in these alloys is attributed to the formation of basal plates. This strengthening effect is reduced as the basal precipitates take the form of Mg₁₂Gd₂Ag in the 0.75 at% sample.

Small addition of Ag to Mg-Gd accelerates the age hardening response and suppresses β formation. It also promotes the formation on basal precipitates. The combination of both changes in precipitation improves the strength. As the additions of Ag increase, a ternary MgGdAg phase becomes stable and decreases the aging response. Fig. 19 shows the predicted pseudo-binary phase diagram for the Mg-10Gd-xAg (wt%) system. Ag has a relatively high solubility in the Mg matrix and Mg₅Gd. This supports the findings of Nie and Gao on a Mg-6Gd-2Ag-0.6Zr (wt%) alloy and Yamada et al. on a Mg-18.7Gd-0.3Zr (wt%) alloy. They found that only metastable basal precipitates form in most of the alloys, but if enough Ag is added a ternary MgGdAg phase will form. Further investigation is needed since the observed ternary phase, Mg₁₂Gd₂Ag, differs from the predicted GdAgMg₁₁. Although the specific ternary phase that forms is likely dependent on the alloy composition. Strengthening increased with Ag additions until the formation of the ternary phase.

4. LPSO strengthening

In addition to the excellent precipitation strengthening options for Mg-RE alloys, the ability to form long period stacking ordered (LPSO) phases has presented a promising avenue for high strength alloys. The LPSO structure was first characterized by Luo et al. [47,48] and major interest came after work by Kawamura et al. [49] who reported that alloys with a TYS of \sim 600 MPa could be obtained using rapidly solidified powder metallurgy techniques. For cast Mg alloys, which usually do not exceed a UTS of 300 MPa, the prospect of such significant strengthening was exciting. Unfortunately, the processing method Kawamura et al. used to produce these LPSO-containing alloys greatly influenced the mechanical properties and are challenging for industrial scale production. Thus, the last 20 years of research has focused on capitalizing on this potential using standard casting and thermo-mechanical processing methods. This review will focus on the effects of LPSO morphology, phase fraction, and formation on the mechanical properties of cast alloys. There has also been significant work on wrought alloys, but that is outside the scope of this review.

4.1. LPSO phase formation and strengthening mechanisms

The LPSO phases in Mg alloys are composed of regularly alternating blocks of HCP Mg layers and blocks of RE and transition metal (TM) enriched FCC layers [50]. The LPSO polytype depends on the number of Mg layers that intersperse

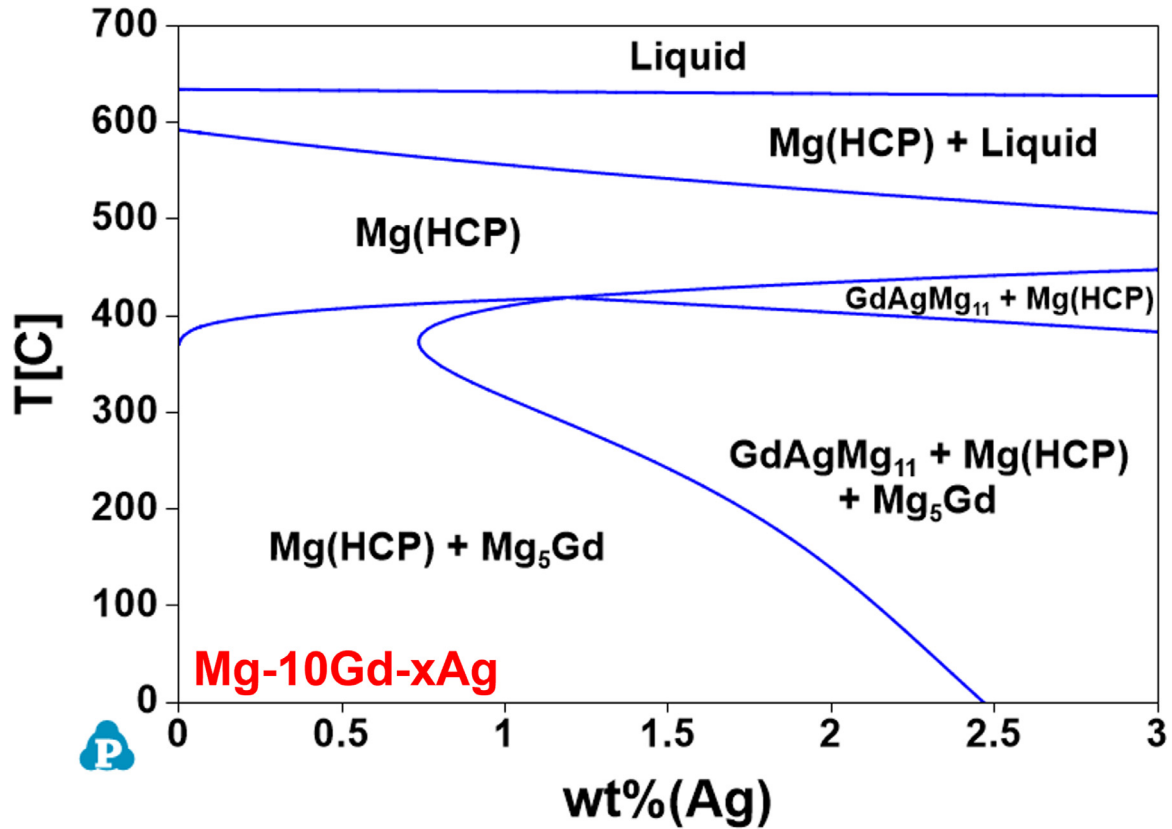


Fig. 19. Predicted pseudo-binary phase diagram of the Mg-10Gd-xAg (wt%) system.

the enriched blocks [50–52], as shown in Fig. 20 [52]. The formation of the enriched building blocks, or structural units as shown in Fig. 20c, is caused by the difference in atomic radius of the RE and TM atoms. The larger RE atoms create a compressive lattice strain around them, while the smaller TM atoms create a tensile lattice strain around them [53–55]. To reduce the overall lattice strain, the RE and TM atoms segregate to the same atomic planes. This segregation lowers the stacking fault energy and results in the local FCC structure bounded by Shockley partial dislocations [5,50,56].

The LPSO structure does not form for all combinations of RE and TM. Four criteria for LPSO formation were established by Kawamura et al. [57] as:

- (1) The mixing enthalpies for the Mg-RE and TM-RE binary systems must be negative;
- (2) The RE must have an HCP crystal structure at room temperature;
- (3) The solid solubility of the RE must be above 3.75 at% in the Mg-binary; and
- (4) The atomic size of the RE must be 8.4% to 11.9% larger than Mg.

If these criteria are met, the different LPSO polytypes can form depending on the alloy composition and thermal processing. As shown in Figs. 5 and 10, a system can form multiple LPSO polytypes and they can stable simultaneously. For a more detailed overview on the specific structure and

formation of the different LPSO phases starting from the first major LPSO publication in 2001 [49], see the 2012 review published by Lu et al. [9].

In terms of CALPHAD predictions, the LPSO phases have previously been described as a stoichiometric compound. In the 2020 PanMagnesium database [26] and the ThermoCalc TCMG6 [25] the LPSO 14H phase was defined as $Mg_{70}(Y,Gd)_8Zn_6$ and $Mg_{88}(Y,Gd)_6Zn_6$, respectively. More recent research has indicated that there is some solid solubility range within the LPSO phases [58,59]. Further investigation is required to determine the most accurate way to define the LPSO phase compositions for the thermodynamic description.

4.2. LPSO strengthening mechanisms

To better understand the strengthening mechanisms of the LPSO, a quick review of deformation in HCP materials is necessary. Due to the HCP structure of Mg, the predominate slip mode is along the basal plane and there is a much higher critical resolve shear stress (CRSS) for the activation of non-basal slip [60]. To accommodate the strain associated with deformation, Mg forms $\{10\bar{1}2\}$ twins [60]. As a result, basal slip and twinning are the primary deformation modes in Mg. While twin formation improves the ductility of Mg, it also affects the TYS and UTS [60]. As discussed in Barnett's 2007 review on twinning, the $\{10\bar{1}2\}$ twins observed in Mg alloys allow deformation along the c-axis of the HCP crystal. Thus, changes to the CRSS of non-basal slip, which have all have a

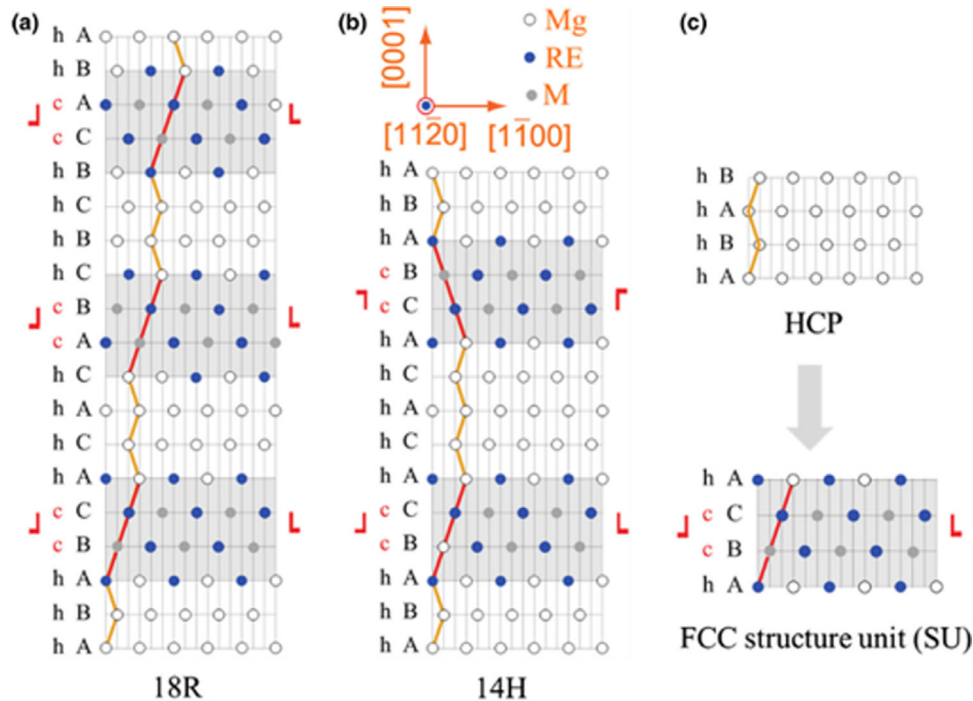


Fig. 20. Stacking sequence of the LPSO (b) 14H and (a) 18R polytypes [52]. The atoms are represented (b) by colored circles: white is Mg, blue is RE, and grey is the transition metal labeled M. (c) shows the transition of the HCP lattice into the enriched FCC structural unit.

c-component in HCP systems, are going to change the activation for twinning as well [61]. The LPSO structure provides strengthening in three major ways: (1) twin suppression, (2) promotion of non-basal slip, and (3) the formation kink bands [9].

It has been observed in LPSO-containing alloys that twins are either not present or are concentrated at grain boundaries [62]. When twins are present, they generally do not propagate across the entire grain [62]. Shao et al. interpret this to mean that the LPSO phases suppress twin propagation instead of nucleation [62]. The mechanism for this relates to the unique stacking of the LPSO structure and the change in crystal structure. Looking back at the LPSO structure in Fig. 20, we can see that the enriched layers run parallel to the basal plane. Thus, the stacking fault, and change in crystal structure, are along the c-axis of the HCP lattice. As a twin tries to propagate, and the lattice reorients along the c-axis, it will encounter the change in crystal structure. To propagate through the FCC region, the twin must convert the stacking fault back into the original HCP structure (e.g. glide of Shockley partial dislocations along the basal plane) [63]. It has been observed that twins are able shear through thinner LPSO plates (< 5 nm in thickness), but as more layers of the LPSO are present (plates thicker than 12 nm) it becomes too energy intensive to shear the plates. As a result, the twins are deflected parallel to the basal plane of the LPSO, where they are often arrested [63,64].

With the suppression of one of the major deformation modes in HCP, the other strengthening mechanisms can be considered. Activation of non-basal slip in HCP materials is associated with both an increase in strength and ductility

[9,60,65]. For non-basal slip to occur, the CRSS of basal slip must be increased to be close to the CRSS to active non-basal slip. The observation of prismatic and pyramidal dislocations in LPSO-containing grains indicates the LPSO structure is impeding basal slip enough to activate these slip modes [9,65].

The final of the three strengthening mechanisms may be the most important: kink band formation. The mechanisms of kink formation are not fully understood and still an active area of research, but the following proposed by Hess and Barrett will provide a sufficient understanding for this review [66]. Similar to twinning, kinks form to accommodate strain in the lattice. In the case of kinks, elastic buckling occurs at a region of localized strain and a pair of opposite sign dislocations form on the basal plane. The dislocations move away from each other in an avalanche effect that results in a progressive rotation of the lattice [66]. This lattice rotation forms the kink and can be thought of as a way for the lattice to reorient so basal dislocation can occur for the loading direction [67]. In LPSO-containing alloys, the formation of kinks refines the LPSO structure and the kink boundaries impede dislocation motion [66]. Combined with the reorientation of the lattice, kinks provide strengthening opportunities and improvements in ductility. The kinking mechanisms of LPSO-containing alloys are of particular interest for wrought alloys since they also suppress micro-cracking and affect dynamic recrystallization [68].

4.3. LPSO microstructure and properties

Although there are different polytypes, research has indicated that the morphology of the LPSO phases has more

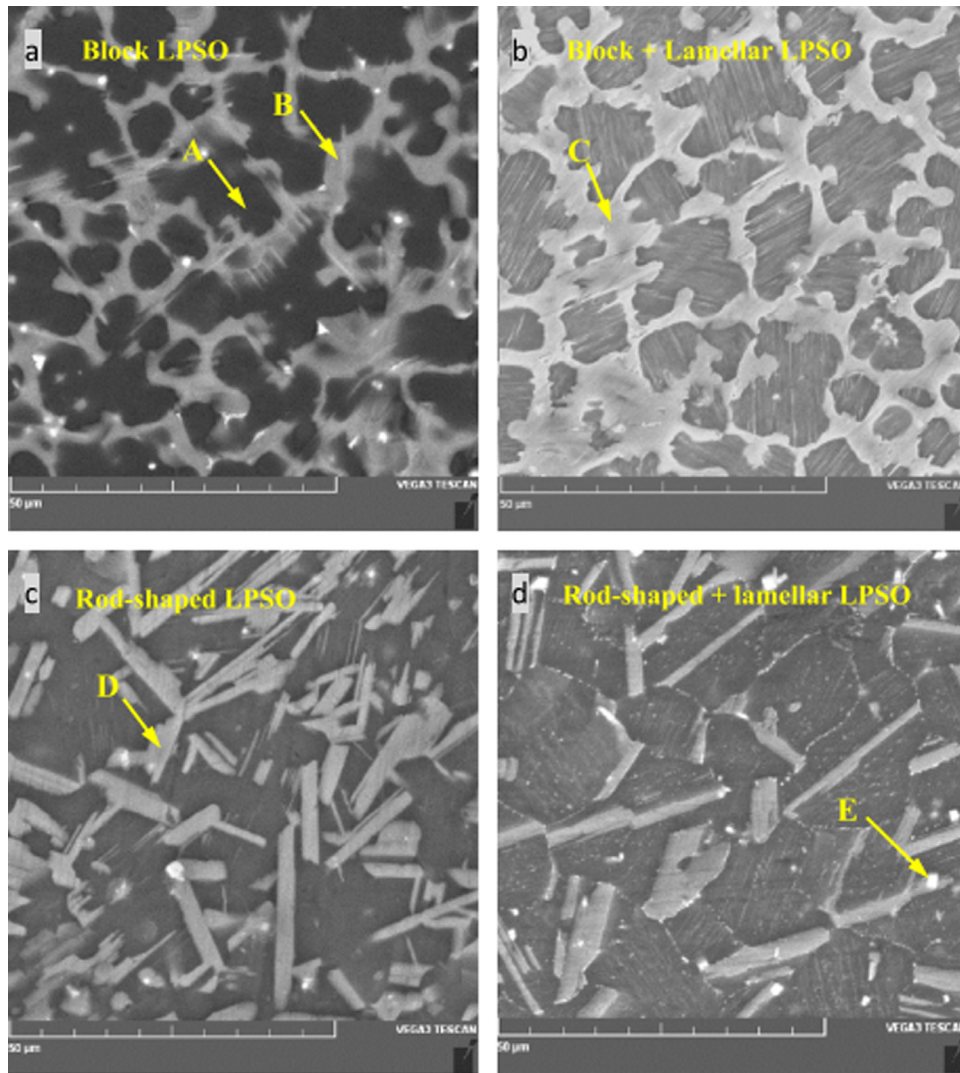


Fig. 21. Examples of the possible LPSO morphologies in a Mg_{95.3}Zn₂Y_{2.7} (at%) alloy in different heat treatment conditions. The blocky LPSO was observed in this alloy in the (a) as-cast state and after heat treatment at (b) 400 °C for 10 h. The rod shaped LPSO formed after a heat treatment at (c) 540 °C for 4 h and after a two-stage heat treatment at (d) 540 °C for 4 h followed by 400 °C for 10 h. The lamellar morphology (b and d) is seen in the sample with heat treatments at 400 °C for 10 h [69].

influence on mechanical properties than the specific stacking. This review will focus on the three major LPSO morphologies (blocky, lamellar, and rod-shaped) and how they affect the mechanical properties of Mg alloys. There will also be a brief review of how each morphology is formed. Examples of each morphology can be seen in Fig. 21.

According to Lu et al. [9], type I LPSO phases, which forms during solidification, can be found in the Mg-Zn-Y, Mg-Zn-Dy, Mg-Zn-Er, Mg-Zn-Ho, and Mg-Zn-Tm ternary systems. Type II LPSO phases form in the Mg-Zn-Gd and Mg-Zn-Tb systems during heat treatment and will be discussed later. It has been determined that LPSO 14H in the Mg-Zn-Gd and Mg-Zn-Y ternary systems can be either type I or II, depending on alloy composition and casting parameters [56,70,71]. The first morphology type is the blocky LPSO phase that is found at the grain boundaries or inter-dendritic regions of solidification microstructure (Fig. 21a and b). Dur-

ing casting, there is segregation of RE and TM atoms to the liquid as the α -Mg forms. This high solute concentrations result in the formation of LPSO directly from the melt as the remaining liquid metal solidifies [19,72]. Consequently, the blocky morphology can be considered a type I morphology. The blocky LPSO generally takes the form of the 18R polytype, but this can vary depending on alloy systems, cooling rate, and compositions [72]. Heat treatment within certain temperature ranges, depending on composition, can lead to a change from the 18R polytype to the 14H polytype. 14H is more stable at lower temperatures [5,9,28]. This transformation may or may not be accompanied by a morphological change as well.

With heat treatment or slower cooling rates during solidification, the other LPSO morphologies can form. The lamellar LPSO morphology consists of fine filament-like LPSO that is imbedded in the α -Mg grains (Fig. 21b and d) [69]. It is

oriented parallel to the basal plane of each grain and is often seen originating from the blocky LPSO at the grain boundaries [69]. Lamellar LPSO forms through a diffusional process. During heat treatment or solidification with slow cooling rates RE and TM atoms are able to diffuse into the α -Mg grains [69,72]. The mechanism for the actual formation is under debate, but a recent article Mao et al. proposed the following mechanism [56]. As RE and TM atoms diffuse, they segregate to two adjacent basal layers in the HCP Mg, which can minimize the elastic strain caused by the difference in atomic size. To further reduce the local free energy, a stacking fault forms by the movement of two Shockley partial dislocations. The resulting structure in the RE and TM enriched region in a block of four planes with a local FCC structure. The formation of the stacking faults then attracts more RE and TM to segregate to the region and the LPSO phase grows. Previously proposed mechanisms are similar but suggest the stacking fault occurs first [53]. The mechanism proposed by Mao et al. is supported by the formation of γ'' precipitates during the early stages of isothermal aging without the formation of stacking faults [73].

The use of the term rod-shaped LPSO morphology varies in literature. In some cases, it is used to refer to very fine lamellar LPSO and in others it is used to describe a thick morphology at or near the grain boundaries. For this review, rod-shaped LPSO will refer to the LPSO morphology with mixed or disorderly orientation to the matrix and is substantially thicker than the lamellar LPSO morphology that forms as a result of high temperature heat treatment [69,74]. An example of this specific rod-shape morphology is shown in Fig. 21c and d. The formation process of the rod-shape LPSO is reported to occur through a few possible mechanisms, all of which may actually happen depending on the exact conditions. The first is similar to the formation of the lamellar LPSO. As a SSSS forms in α -Mg grains during a heat treatment, RE and TM atoms segregate and stacking faults are formed [75]. The second mechanism is the transformation of the blocky LPSO to the rod-shaped LPSO. In most of the LPSO-forming systems, the 18R phase is observed to form during solidification, but it is less stable than the 14H as the temperature decreases [5,9,28]. During heat treatment, diffusion can occur and the less stable LPSO 18R blocky phase will transform into the more stable LPSO 14H rod-shaped phase [69,73,74]. The exact mechanism of this polytype transformation has not been described and needs further study. It is possible that the transformation from the blocky 18R to the blocky 14H is similar to the spinodal decomposition [76].

In terms of mechanical properties, the LPSO morphology is important for two major reasons: thickness of the LPSO and stress concentration. As previously discussed, in order for twins to propagate through the LPSO they must either shear the enriched FCC layers or move as Shockley partials. In other words, it is easier for the twin or dislocation to propagate through a thinner LPSO morphology than a thicker one. The blocky LPSO is consistently the thickest morphology and has been reported to have the highest strength [69,74,77,78]. Being much thinner, the lamellar LPSO is not able to stop

dislocation motion or twinning in the same way and thus provides less strengthening. The formation of the lamellar LPSO also results from the dissolution of the blocky LPSO, so the overall mechanical properties are lower with its formation [78]. The strengthening effect of each morphology is reported as (from high to low):

blocky > rod – shaped > lamellar > veryfinelamellar

Higher volume fraction of blocky LPSO morphology is also reported to improve the flow stress, dynamic recrystallization, and workability of extruded alloys [77]. The rod-shaped LPSO is reported to increase the dampening properties of the alloy while maintaining relatively high mechanical properties [69]. In the case that there is a combination of blocky and lamellar LPSO morphologies, the formation of the lamellar morphology has been observed to reduce the ductility [69,78]. This indicates the blocky LPSO may have greater ductility than the lamellar.

The other factor affecting the mechanical properties for LPSO-containing alloys is stress concentration. As the volume fraction of blocky LPSO increases, it forms a discontinuous network at the grain boundaries. Micro-cracks were found at the interface between the LPSO and Mg matrix, which indicates stress is being concentrated at that interface [74]. Cheng et al. reported that dense lamellar LPSO constrains the grains and concentrates stress when the deformation is incompatible between adjacent grains [74]. In comparison, the rod-shaped LPSO generally has a smaller average size and better dispersion. Micro-cracks are suppressed by the formation of kink banding in the rod-shaped LPSO [74]. Thus, the promotion of kink banding aids in improving the ductility and strength.

4.4. Modification of LPSO morphology

Since the LPSO morphology can distinctly affect the mechanical properties of Mg-RE based alloys containing LPSO phases, tailoring it to the application is attractive in Mg alloy design and processing. The LPSO morphology can be changed in the following two main ways: thermal processing and alloying additions.

4.4.1. Thermal processing (heat treatment)

Thermal processing can include solution/homogenization treatments, aging heat treatments, and variation in cooling rates. As a result, CALPHAD modeling can be a powerful tool in choosing appropriate temperatures for thermal processing. For general phase stability and phase fractions, two models can be used to predict a system: the equilibrium and Scheil models. As the name suggests, the equilibrium model describes the equilibrium state where diffusion is assumed to be infinite in the system [79]. In the Scheil model, it is assumed that diffusion is infinite in liquid but there is no diffusion in solid. Thus, the Scheil model can be used to estimate the microconstituents in the as cast microstructure, with one major caveat. The Scheil model best represents conditions with very fast cooling, so slower cooling may result in deviation from the model because diffusion occurs in the solid

[79]. The combination of these two models can be used to select heat treatment conditions to promote different phases. At this time there is no way to differentiate between the LPSO morphology types by only using CALPHAD modeling.

At higher temperatures, generally above ~ 500 °C, several major changes can occur in microstructure of Mg-RE based alloys: (1) less stable secondary phases dissolve [75,76], (2) blocky morphology can thicken [73,80], and/or (3) blocky morphology can transform into the rod-shaped morphology [69,74,76]. There are some reports that the lamellar LPSO can form in this temperature range as well, but they are less common [76]. At lower temperatures, generally below ~ 450 °C, there is some dissolution of the blocky morphology and the formation of the lamellar morphology [69,74–76,78].

Yuan et al. also explored a way of continuous and discontinuous cooling which affected the LPSO morphology [73]. They found that a slower continuous cooling rate (i.e., there is more time for diffusion) resulted in coarsening of the blocky LPSO and growth of the lamellar phase. With discontinuous cooling, the blocky morphology becomes more discontinuous as the cooling rate changes and the rod-shaped morphology is promoted [73].

4.4.2. Alloying additions

Alloying elements have a significant influence on the precipitation of the LPSO phase and are necessary to obtain certain properties. As alloying is done to promote grain refinement or precipitation hardening, the effects on the LPSO morphology must be considered. Extensive study has already been reported on the effects of Zn additions and the RE/Zn ratio [8,11,12,81–83], so this review will only give a brief overview of Zn alloying and introduce three other alloying elements: Zr, Mn, and Nd.

In general, increasing the Zn content in Mg-RE alloys promotes the formation of all the LPSO morphologies [76–78,80]. As the Zn content increases, the LPSO becomes more stable up to the RE/Zn ratio where the W-phase starts to form. For more detail on the phase stability in the Mg-Gd-Zn and Mg-Y-Zn systems, see the works by Luo et al. and Gröbner et al. [8,14,84]. In the LPSO forming regions, increasing Zn results in an increase in the overall LPSO volume fraction [76,77,80]. Specifically, there is an observed increase in the blocky LPSO in the as-cast and at higher temperatures (greater than ~ 500 °C) [77]. There is also an observed increase in dissolution of the blocky LPSO and precipitation of the lamellar morphology at lower temperatures (less than ~ 500 °C) in some alloys [78]. The specific response varies depending on the RE/Zn ratio.

Mg alloys tend to form large grains from casting and grain growth during heat treatments. Grain refiners are often used to cause heterogeneous nucleation of grains during solidification and to pin grain boundaries during heat treatment. The most commonly used grain refiner in Mg alloys is Zr [85,86]. In a study by Zhang et al., it was found that increasing the Zr content in an Mg-0.5Zn-1Y-xZr ($x = 0, 0.1, 0.2,$ and 0.3 at%) alloy results in a decrease in the LPSO formation in the as-cast condition [87]. As the Zr increased from 0.1 to 0.2

at%, the lamellar LPSO decreases and becomes more discontinuous. A further increase to 0.3 at% resulted in an almost complete disappearance of the lamellar LPSO and the remaining blocky morphology becomes finer and more dispersed. The proposed mechanism for the LPSO suppression is that the Zr increases the stacking fault energy and the energy for nucleation and growth of the LPSO [87].

A less commonly used grain refiner in Mg alloys is Mn. Unlike the Zr additions, Mn was found to promote LPSO precipitation [88]. It was also found that Mn promotes the formation of $(\text{Mg,Zn})_3\text{RE}$ during solution treatment at 500 °C. In this study, the solution treatment was 1000 h, so the overall morphology tended toward the lamellar LPSO. More study should be done to determine the LPSO morphology for shorter aging times.

Nd also presents itself as an interesting alloying addition due to the formation of β -series precipitates similar to the Mg-Gd system, as discussed above. Nd is not an LPSO-forming RE element, so it has the potential to provide precipitation strengthening without depleting the rare earths for LPSO formation. This will be discussed in more detail later. In several studies focusing on LPSO formation, it was found that Nd suppresses LPSO formation during solidification [89,90]. Also, Nd was found to promote the precipitation of Mg_3RE and Mg_5RE [89,91,92]. With solution treatment, Nd additions resulted in a finer, more uniform LPSO morphology and it prevented coarsening [90]. As a result, using Nd for β -series precipitation may result in complications with LPSO formation. It has also been reported that Nd additions can refine and help homogenize the as-cast microstructure [92].

4.5. Other phases in LPSO-forming alloys

Although the formation of LPSO phases can provide significant strengthening, the coprecipitation of other secondary phases can be advantageous to mechanical properties. In the LPSO forming systems there are two major secondary phases that can form: W-phase and β -series, and γ -series precipitates.

The W-phase ($\text{Mg}_3\text{RE}_2\text{Zn}_3$) is a generally hard and brittle secondary phase found in Mg-RE-Zn alloys with higher Zn contents [93]. It has in the past been confused with the $(\text{Mg,Zn})_3\text{RE}$ phase [76] due to the fact they have the same crystal structure. The difference between the two phases is in the atoms occupying 8c lattice site and the morphology [14,94]. In terms of mechanical properties, W-phase can provide some strengthening due to its higher hardness than that of Mg matrix. If it is small in size the strength of alloys can be improved, especially in combination with blocky LPSO phases [76,78]. This improvement can also be seen in the as-extruded state where the W-phase is fragmented into smaller pieces [95]. Coarser net-shaped W-phase starts to degrade the mechanical properties since it can serve as a stress concentration site and there is weak bonding with the α -Mg matrix [76,96]. It has been proposed that if the phase fraction of W-phase is greater than 17.5 vol% there will be a decrease in

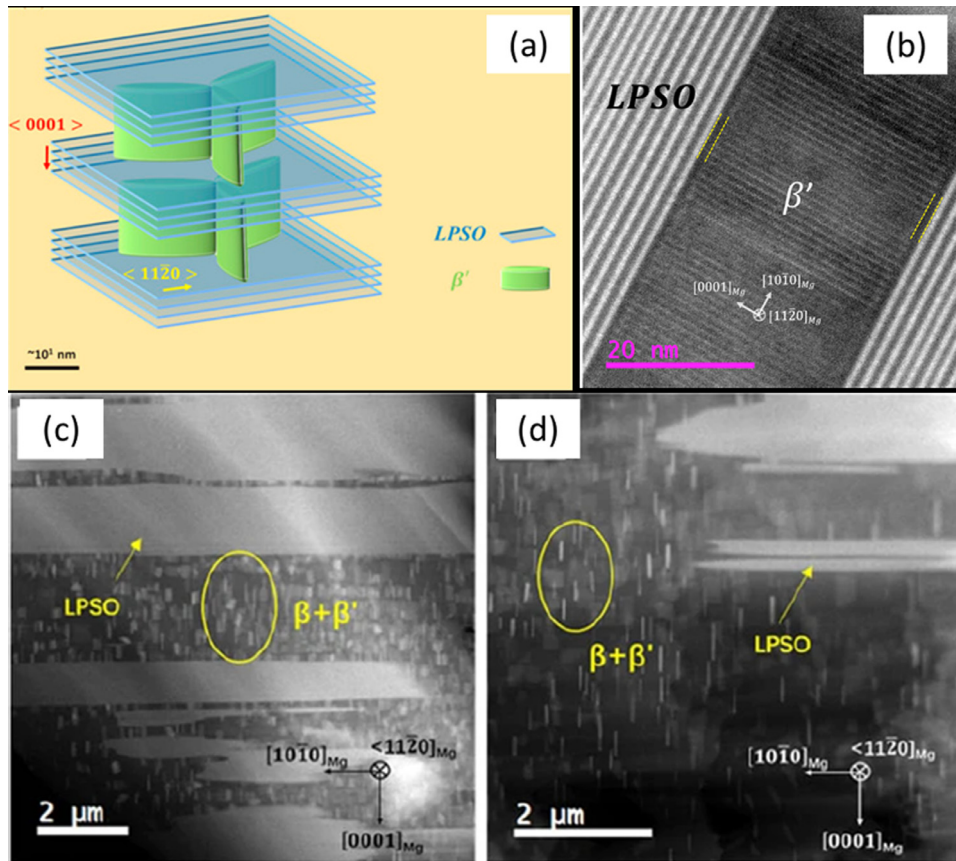


Fig. 22. Representative examples of the 3-D network microstructure formed by LPSO and β -series precipitates as an (a) illustration [102] and (b) with atomic resolution HAADF-STEM of an Mg-10Gd-5Y-2Zn-0.5Zr (at%) alloy homogenized at 500 °C for 5 h, water quenched, and aged at 225 °C for 48 h [102]. Images (c) and (d) are HAADF-STEM images of an Mg₉₆Gd₂Y₁Ni₁ (atomic ratio) alloy homogenized at 500 °C for 8 h and aged at 200 °C for (c) 4 h and (d) 53 h [103].

mechanical properties [83]. This phase fraction likely varies with alloy composition.

The coexistence of LPSO phases and metastable β -series precipitates (specifically β' and β_1) can be beneficial to mechanical properties of Mg-RE alloys. Early in the study of LPSO-containing alloys, Yamada et al. found that peak-aged Mg-2Gd-1.2Y-xZn-0.2Zr ($x = 0.05$ to 2, at%) alloys contained both LPSO and β' [97]. The coexistence of LPSO, β' , and β_1 results in increase in strength and toughness [98–105]. The addition of TM elements, such as Ag or Zn discussed early in the β -series section, can produce the formation of fine basal γ' (MgREZn) and γ'' (Mg₅(RE,Zn)) precipitates. It should be noted that γ' and γ'' have the same structure as the enriched LPSO building blocks previously discussed. These γ'/γ'' and the LPSO phases form along the basal planes while the β' and β_1 form on the prismatic plates. The resulting microstructure is a 3-D network where β' and β_1 are sandwiched between the LPSO and γ'/γ'' [98,99,101,103,105,106]. A schematic of this 3-D network microstructure and several representative TEM micrographs from literature can be seen in Fig. 22. This 3-D network microstructure impedes dislocation motion and prevents microcracks, thus improving the mechanical properties [103]. In

this microstructure, the β -series precipitates contribute most to the strengthening [104], but a combination of the β' and γ' can exhibit comparable properties to microstructures with only β' [101]. The γ' formation can also improve the ductility of the microstructure [105] while the β' can lead to a reduction in ductility [76].

5. Promising Mg-RE based alloys

Based on the discussions of strengthening mechanisms from precipitation, LPSO and other phases, several promising alloys containing LPSO, β -series, and γ -series precipitates, reported in literature, are summarized in Tables 1, in comparison with commercial alloys WE43 and WE54.

Table 1 lists the composition, process condition, microstructure (phases), and room-temperature mechanical properties of several experimental alloys. CALPHAD predicted LPSO and β phase fractions for these alloys are also listed for reference. Since the predictions are for the equilibrium condition, metastable phases are not directly assessed; however, the predicted equilibrium β phase fractions can be used as an estimation for the metastable β' phase fraction. An initial comparison in Table 1 shows an interesting lack of

Table 1
 Microstructure and room-temperature mechanical properties of experimental Mg-RE based cast alloys in comparison with commercial alloys WE43 and WE54. In the WE43 and WE54 alloys, RE is a 50 wt% Nd mischmetal. For phase fraction predictions, RE is replaced by Nd for the WE alloys. Italic text indicates composition that has been converted to at% or wt% from composition given in literature. β' phase fraction was estimated by summing the predicted equilibrium β (Mg_5Gd , $Mg_{41}Nd_5$, $Mg_{24}Y_5$) fractions. Abbreviations: air cooled (AC), water cooled (WC), water quenched (WQ), tensile yield strength (TYS), ultimate tensile strength (UTS), and E_f (tensile elongation at fracture).

Composition (wt%)	Composition (at%)	Process condition			Reported LPSO	TYS (MPa)	UTS (MPa)	E_f (%)	Hardness (HV)	Predicted phase fraction (vol%)		Reference
		As-Cast	Homogenization	Aging						LPSO	β'	
Mg-4Y-1Gd-1Nd-1Zn-0.3Zr	Mg-1.15Y-0.16Gd-0.53Nd-0.39Zn-0.08Zr	Cast into water cooled mold	500 °C/10 h/AC	200 °C/120h	Mostly lamellar	135	260	26.9	90	7.18%	3.94%	[101]
			500 °C/10 h/WC	200 °C/72h	More blocky than lamellar	135	249	26.4	79	7.18%	3.94%	
Mg-4Y-1Gd-1Nd-1Zn-0.4Ca-0.3Zr	Mg-1.15Y-0.16Gd-0.53Nd-0.39Zn-1.01Ca-0.08Zr		500 °C/10 h/AC	200 °C/120h	Mostly lamellar	140	234	11.1	84	7.18%	4.06%	
			500 °C/10 h/WC	200 °C/72h	Some blocky, some lamellar, some rod-shaped	153	264	17.2	81	7.18%	4.06%	
Mg-6Gd-3Y-1Zn-0.4Zr	Mg-1Gd-0.89Y-0.4Zn-0.12Zr	Direct chill casting	510 °C/24 h/WQ	200 °C/96h	More blocky than lamellar	184	250	3.3	100	7.56%	5.96%	[105]
Mg-6Gd-3Y-1Zn-0.3Ag-0.4Zr	Mg-1Gd-0.9Y-0.41Zn-0.07Ag-0.12Zr			200 °C/72h	Mostly lamellar	218	292	4.4	112	8.53%	6.80%	
Mg-4.5Y-2.5Nd-1.0Gd-0.5Zn-0.5Zr	Mg-1.31Y-1.35Nd-0.16Gd-0.2Zn-0.14Zr	Metal mold casting	520 °C/12h	200 °C/42h	No LPSO, only γ''	~235	~327	~3.9	118	3.72%	9.39%	[100]
Mg-10Gd-3.5Er-0.5Zn-0.5Zr	Mg-1.74Gd-0.58Er-0.21Zn-0.15Zr	Steel mold casting	520 °C/6 h/WQ(70 °C)	225 °C/128h	Lamellar	216	296	6.4	99.7	0.08%	12.50%	[104]
Mg-12Gd-2Er-1Zn-0.6Zr	Mg-2.11Gd-0.33Er-0.43Zn-0.18Zr	Steel mold casting	520 °C/24 h/WQ(hot)	225 °C/84h	Lamellar	313	335	2.7	188	2.73%	11.97%	[107]
Mg-14.10Gd-2.32Zn-0.52Zr	Mg-2.5Gd-1Zn-0.16Zr	Semi-continuous casting	520 °C/12 h/WQ(hot)	200 °C/64h	Fine lamellar	292	404	5.3		11.95%	8.80%	[108]
Mg-14Gd-3Y-1.8Zn-0.5Zr	Mg-2.53Gd-0.97Y-0.79Zn-0.16Zr	Permanent mold casting	520 °C/10 h/WQ(70 °C)	225 °C/16h	More blocky than lamellar	230	366	2.8	127	14.27%	12.86%	[109]
Mg-16.5Gd-2.26Zn-0.63Zr	Mg-3Gd-1Zn-0.2Zr	Steel mold casting	500 °C/12 h/WQ(80 °C)	200 °C/30h	More blocky than lamellar	242	345	5.4		10.88%	12.48%	[110]
Mg-16.47Gd-2.26Zn-0.95Zr	Mg-3Gd-1Zn-0.3Zr			200 °C/30h	Mostly lamellar	262	332	2.1		10.88%	12.48%	
Mg-15Gd-1Zn-0.4Zr	Mg-2.66Gd-0.43Zn-0.12Zr	Steel mold casting	520 °C/12 h/WQ(90 °C)	200 °C/64h	No LPSO, only γ'	288	405	2.9	127	2.07%	14.55%	[111]
WE43 (Mg-4Y-3.4RE-0.7Zr)	WE43 (Mg-1.15Y-1.82RE-0.2Zr)	Sand mold	525 °C/6 h/WQ(hot)	250 °C/16h	No LPSO, only β'	185	250	2	96	0.00%	9.27%	[112]
WE54 (Mg-5.2Y-3RE-0.7Zr)	WE54 (Mg-1.51Y-1.62RE-0.2Zr)	Sand mold	525 °C/8 h/WQ(hot)	250 °C/16h	No LPSO, only β'	205	250	2	96	0.00%	11.12%	[112]

a larger relationship between the thermal processing, predicted LPSO fractions, and LPSO morphology. The LPSO morphology appears to be more directly related to the specific composition and thermal processing than a larger trend. There is also not an obvious trend between the LPSO morphology and mechanical properties based on the experimental results. This does not support some of the previously discussed trends that associate blocky LPSO with higher strength.

Other interesting trends between the phase fraction and mechanical properties can be seen in Table 1. The alloys with the highest TYS tend to have a relatively high predicted β' fraction while the LPSO phase fraction varies. The alloys with a relatively high volume fraction of both LPSO and β' tended to have the highest UTS. The alloys with the highest elongation tended to have moderate LPSO fraction and low relative β' prime fractions. There are some exceptions to each case, but this analysis does not account for other factors such as grain size. This indicates that the mechanical properties are more dependent on the β' than on the LPSO phase fraction and morphology.

Table 1 also suggests that the combination of LPSO and β' phases can provide higher strength than those of commercial WE54 and WE43 alloys with only β series strengthening. Another advantage of combined LPSO and β' microstructure is the resistance to over aging. Normally during isothermal aging, β' and β_1 precipitates coarsen with time. In this case, the LPSO, γ' , and/or γ'' run perpendicular to the growth direction of the β' and β_1 . The LPSO and γ' are thermally stable at lower temperatures used for age hardening (usually less than 250 °C), and do not usually change/dissolve while the β -series precipitates are forming. When the β' and β_1 precipitates encounter these basal structure they are unable to continue growing along the preferred $[0001]_a$ direction. As a result, the coarsening of the β' and β_1 is prevented [99,102,103,106]. This resistance to β' and β_1 coarsening opens up possibilities for higher strength alloys and elevated temperature applications.

Unfortunately, there is competition between the formation of the LPSO and β -series precipitation since both contain RE elements [76,101]. As previously discussed, for β -series precipitates to form, there needs to be a SSSS in the matrix. The formation of the LPSO and γ' depletes the RE concentrations in the matrix [76,80,101]. In addition, alloying elements, such as Zn or Nd, can affect the precipitation [89,100,104]. At lower concentrations, Zn can refine β' precipitates [100], but with an increase in Zn additions, more of the LPSO forms and the number density of β' precipitates is reduced. [80,100]. As a result, there is a decrease in formation of β' and the average size of the β' precipitates is larger [76,80]. As shown in Table 1, high volume fractions of both LPSO and β' can be achieved, but a high RE concentration is required.

A potential way around this depletion of RE by LPSO formation is to use a different RE β -series. As discussed, Nd also forms β -series precipitation in Mg, but it also can suppress the formation of LPSO during solidification. That indicates

there are more factors when designing Gd and Nd containing alloys that need to be studied further. Other options, include microalloying with elements like Ag or Ca that refine and/or promote β -series precipitation [101,105].

6. Summary and future outlook

In the past 20 years, extensive research has been done into developing new Mg-RE based cast alloys. The precipitation of binary Mg-Gd and Mg-Nd metastable β -series phases has opened up opportunities for high-strength applications. This precipitation can be modified by micro-alloying with elements such as Zn, Ca, and Ag, to increase the number density of β' and β_1 precipitates and/or promote the formation of basal γ -series precipitates. Many promising new alloys have been developed, but more work is needed to assess the effects of other common alloying additions. Particularly, the effects of common grain refiners on the β -series precipitates should be assessed in more detail due to their importance in cast alloys.

Larger additions of certain transition metal alloying elements, such as Zn, to certain Mg-RE alloys can lead to the formation of LPSO phases. The unique stacking of the LPSO phases can increase strength and ductility, but the LPSO morphology can play an important role in strengthening mechanisms. Despite some conflicting reports, the blocky morphology that forms during solidification or at higher temperatures generally contributes more to strengthening than the lamellar morphology that forms at temperature lower than ~ 450 °C. There is some evidence that the formation of the lamellar morphology in addition to the blocky morphology can result in a reduction in ductility. Micro-alloying and thermal processing can also be used to modify the LPSO morphology. More work should be done directly comparing the effects of conventionally casting methods and thermal processing to better differentiate the effects of LPSO phase morphology. This would better establish how the microstructure can be tailored in cast for different applications. In addition, the alloys in Table 1 that primarily rely on strengthening from the LPSO phases require a large amount of RE (often >10 wt%) to produce strengthening similar to the alloys that rely on β -series precipitation. The high cost and increased density of many of these alloys highlights the need for the development of more dilute compositions with comparable properties.

Going forward, the combination of β' and LPSO (or the basal γ' building blocks) phases can lead to superior strength and ductility in Mg-RE based cast alloys. The β' and LPSO can form a complex three-dimensional network that effectively impedes dislocation motion on the basal and non-basal planes. The LPSO structure also prevents the coarsening of β' precipitates when they interact, thus providing good thermal stability at elevated temperatures. Further work is needed to determine how the combination of these two phases can be best used in alloy design and manufacturing scale applications.

Acknowledgments

This work was partially funded by the United States Army Research Laboratory (ARL) and Terves LLC. The authors would like to acknowledge Dr. Vincent Hammond of ARL and the members of Lightweight Materials and Manufacturing Laboratory at The Ohio State University (OSU) for their insightful discussions. This material is based upon work supported by the Army Contracting Command - Adelphi, MD under Contract No W911QX-18-P-0038. Any opinions, findings and conclusions or recommendations expressed in this material are those of the author(s) and do not necessarily reflect the views of ARL. CompuTherm and Thermo-Calc are gratefully acknowledged for providing long time support to our CALPHAD software and related databases, and many helpful discussions with Professor Rainer Schmid-Fetzer of Clausthal University of Technology over the years.

References

- [1] A.A. Luo, *Int. Mater. Rev.* 49 (2004) 13–30, doi:[10.1179/095066004225010497](https://doi.org/10.1179/095066004225010497).
- [2] Z. Yang, J.P. Li, J.X. Zhang, G.W. Lorimer, J. Robson, *Acta Metall. Sin.* 21 (2008) 313–328 English Lett., doi:[10.1016/S1006-7191\(08\)60054-X](https://doi.org/10.1016/S1006-7191(08)60054-X).
- [3] H. Si, Y. Jiang, Y. Tang, L. Zhang, *J. Magnes. Alloy.* 7 (2019) 501–513, doi:[10.1016/j.jma.2019.04.006](https://doi.org/10.1016/j.jma.2019.04.006).
- [4] C. Zhu, B. Chen, *Adv. Eng. Mater.* 21 (2019) 1–23, doi:[10.1002/adem.201800734](https://doi.org/10.1002/adem.201800734).
- [5] A.A. Kaya, *Front. Mater.* 7 (2020) 1–26, doi:[10.3389/fmats.2020.00198](https://doi.org/10.3389/fmats.2020.00198).
- [6] Q. Luo, Y. Guo, B. Liu, Y. Feng, J. Zhang, Q. Li, K. Chou, *J. Mater. Sci. Technol.* 44 (2020) 171–190, doi:[10.1016/j.jmst.2020.01.022](https://doi.org/10.1016/j.jmst.2020.01.022).
- [7] K.W. Guo, *Recent Pat. Corros. Sci.* 2 (2010) 13–21, doi:[10.2174/1877610801002010013](https://doi.org/10.2174/1877610801002010013).
- [8] J. Gröbner, A. Kozlov, X.Y. Fang, J. Geng, J.F. Nie, R. Schmid-Fetzer, *Acta Mater.* 60 (2012) 5948–5962, doi:[10.1016/j.actamat.2012.05.035](https://doi.org/10.1016/j.actamat.2012.05.035).
- [9] F. Lu, A. Ma, J. Jiang, D. Yang, Q. Zhou, *Rare Met.* 31 (2012) 303–310, doi:[10.1007/s12598-012-0510-y](https://doi.org/10.1007/s12598-012-0510-y).
- [10] J.F. Nie, *Metall. Mater. Trans. A Phys. Metall. Mater. Sci.* 43 (2012) 3891–3939, doi:[10.1007/s11661-012-1217-2](https://doi.org/10.1007/s11661-012-1217-2).
- [11] J. Gröbner, A. Kozlov, X.Y. Fang, S. Zhu, J.F. Nie, M.A. Gibson, R. Schmid-Fetzer, *Acta Mater.* 90 (2015) 400–416, doi:[10.1016/j.actamat.2015.02.044](https://doi.org/10.1016/j.actamat.2015.02.044).
- [12] J. Gröbner, S. Zhu, J.F. Nie, M.A. Gibson, R. Schmid-Fetzer, *J. Alloy. Compd.* 675 (2016) 149–157, doi:[10.1016/j.jallcom.2016.03.106](https://doi.org/10.1016/j.jallcom.2016.03.106).
- [13] F. Pan, M. Yang, X. Chen, *J. Mater. Sci. Technol.* 32 (2016) 1211–1221, doi:[10.1016/j.jmst.2016.07.001](https://doi.org/10.1016/j.jmst.2016.07.001).
- [14] L. Luo, Y. Liu, M. Duan, *Materials (Basel)* 11 (2018) 1351, doi:[10.3390/ma11081351](https://doi.org/10.3390/ma11081351).
- [15] D.R. Lide (Ed.), *CRC handbook of chemistry and physics*, CRC Press, Inc., Boca Raton, Florida, 1994.
- [16] T.M. Pollock, *Science (80-)* 328 (2010) 986–987, doi:[10.1126/science.1182848](https://doi.org/10.1126/science.1182848).
- [17] M. Esmaily, J.E. Svensson, S. Fajardo, N. Birbilis, G.S. Frankel, S. Virtanen, R. Arrabal, S. Thomas, L.G. Johansson, *Prog. Mater. Sci.* 89 (2017) 92–193, doi:[10.1016/j.pmatsci.2017.04.011](https://doi.org/10.1016/j.pmatsci.2017.04.011).
- [18] A. Luo, M.O. Pekguleryuz, *J. Mater. Sci.* 29 (1994) 5259–5271, doi:[10.1007/BF01171534](https://doi.org/10.1007/BF01171534).
- [19] J. Xie, J. Zhang, Z. You, S. Liu, K. Guan, R. Wu, J. Wang, J. Feng, *J. Magnes. Alloy.* 9 (2021) 41–56, doi:[10.1016/j.jma.2020.08.016](https://doi.org/10.1016/j.jma.2020.08.016).
- [20] T.L. Chia, M.A. Easton, S.M. Zhu, M.A. Gibson, N. Birbilis, J.F. Nie, *Intermetallics* 17 (2009) 481–490, doi:[10.1016/j.intermet.2008.12.009](https://doi.org/10.1016/j.intermet.2008.12.009).
- [21] R. Schmid-Fetzer, *J. Phase Equilibria Diffus.* 35 (2014) 735–760, doi:[10.1007/s11669-014-0343-5](https://doi.org/10.1007/s11669-014-0343-5).
- [22] L. Kaufman, H. Mernstein, Academic Press Inc., New York, NY, USA, 1970.
- [23] Y.A. Chang, S. Chen, F. Zhang, X. Yan, F. Xie, R. Schmid-Fetzer, W.A. Oates, *Prog. Mater. Sci.* 49 (2004) 313–345, doi:[10.1016/S0079-6425\(03\)00025-2](https://doi.org/10.1016/S0079-6425(03)00025-2).
- [24] A.A. Luo, *Calphad Comput. Coupling Ph. Diagr. Thermochem.* 50 (2015) 6–22, doi:[10.1016/j.calphad.2015.04.002](https://doi.org/10.1016/j.calphad.2015.04.002).
- [25] Thermo-Calc, Thermo-Calc Software, 2021 <https://thermocalc.com/>.
- [26] CompuTherm, 2021 <https://compuTherm.com/software>.
- [27] CRCTFactSage.com, 2021 <https://www.factsage.com/>.
- [28] D. Wan, H. bin Wang, Z. min Li, Y. lin Hu, J. jun Hu, Y. dan Xue, L. sen Wang, K. jin Fang, *China Foundry* 17 (2020) 42–47, doi:[10.1007/s41230-020-9088-4](https://doi.org/10.1007/s41230-020-9088-4).
- [29] A. Issa, J.E. Saal, C. Wolverton, *Acta Mater.* 83 (2015) 75–83, doi:[10.1016/j.actamat.2014.09.024](https://doi.org/10.1016/j.actamat.2014.09.024).
- [30] J. Zhang, S. Liu, R. Wu, L. Hou, M. Zhang, *J. Magnes. Alloy.* 6 (2018) 277–291, doi:[10.1016/j.jma.2018.08.001](https://doi.org/10.1016/j.jma.2018.08.001).
- [31] A.A. Nayeab-Hashemi, J.B. Clark, ASM International, Materials Park, OH, 1988.
- [32] J.F. Nie, X. Gao, S.M. Zhu, *Scr. Mater.* 53 (2005) 1049–1053, doi:[10.1016/j.scriptamat.2005.07.004](https://doi.org/10.1016/j.scriptamat.2005.07.004).
- [33] J.F. Nie, N.C. Wilson, Y.M. Zhu, Z. Xu, *Acta Mater.* 106 (2016) 260–271, doi:[10.1016/j.actamat.2015.12.047](https://doi.org/10.1016/j.actamat.2015.12.047).
- [34] A.R. Natarajan, E.L.S. Solomon, B. Puchala, E.A. Marquis, A. Van Der Ven, *Acta Mater.* 108 (2016) 367–379, doi:[10.1016/j.actamat.2016.01.055](https://doi.org/10.1016/j.actamat.2016.01.055).
- [35] H. Liu, Y.M. Zhu, N.C. Wilson, J.F. Nie, *Acta Mater.* 133 (2017) 408–426, doi:[10.1016/j.actamat.2017.03.065](https://doi.org/10.1016/j.actamat.2017.03.065).
- [36] Q. Chen, A. Tang, J. Ye, L. Hao, Y. Wang, T. Zhang, *Mater. Sci. Eng. A* 686 (2017) 26–33, doi:[10.1016/j.msea.2017.01.012](https://doi.org/10.1016/j.msea.2017.01.012).
- [37] H. Zhang, J. Fan, L. Zhang, G. Wu, W. Liu, W. Cui, S. Feng, *Mater. Sci. Eng. A* 677 (2016) 411–420, doi:[10.1016/j.msea.2016.09.044](https://doi.org/10.1016/j.msea.2016.09.044).
- [38] Y. Zhou, P. Fu, L. Peng, D. Wang, Y. Wang, B. Hu, M. Liu, A.K. Sachdev, W. Ding, *J. Magnes. Alloy.* 7 (2019) 113–123, doi:[10.1016/j.jma.2019.02.003](https://doi.org/10.1016/j.jma.2019.02.003).
- [39] A. Sanaty-Zadeh, A.A. Luo, D.S. Stone, *Acta Mater.* 94 (2015) 294–306, doi:[10.1016/j.actamat.2015.05.001](https://doi.org/10.1016/j.actamat.2015.05.001).
- [40] X. Gao, J.F. Nie, *Scr. Mater.* 58 (2008) 619–622, doi:[10.1016/j.scriptamat.2007.11.022](https://doi.org/10.1016/j.scriptamat.2007.11.022).
- [41] J. Zheng, Z. Li, Z. Luo, X. Xu, B. Chen, *Adv. Eng. Mater.* 19 (2017) 1–9, doi:[10.1002/adem.201600244](https://doi.org/10.1002/adem.201600244).
- [42] B.Z. Sun, Y. Dong, J. Tan, Y. Tian, J.X. Ren, *Scr. Mater.* 194 (2021), doi:[10.1016/j.scriptamat.2020.11.010](https://doi.org/10.1016/j.scriptamat.2020.11.010).
- [43] L. Shi, Y. Huang, L. Yang, F. Feyerabend, C. Mendis, R. Willumeit, K. Ulrich Kainer, N. Hort, *J. Mech. Behav. Biomed. Mater.* 47 (2015) 38–48, doi:[10.1016/j.jmbbm.2015.03.003](https://doi.org/10.1016/j.jmbbm.2015.03.003).
- [44] H.W. Chen, C.L. Liu, Z.Q. Li, P. Li, A.P. Zhang, J.F. Nie, *Mater. Charact.* 156 (2019), doi:[10.1016/j.matchar.2019.109838](https://doi.org/10.1016/j.matchar.2019.109838).
- [45] N. Mo, I. McCarroll, Q. Tan, A. Ceguerra, Y. Liu, J. Cairney, H. Dieringa, Y. Huang, B. Jiang, F. Pan, M. Birmingham, M.X. Zhang, *Acta Mater.* 181 (2019) 185–199, doi:[10.1016/j.actamat.2019.09.058](https://doi.org/10.1016/j.actamat.2019.09.058).
- [46] K. Yamada, H. Hoshikawa, S. Maki, T. Ozaki, Y. Kuroki, S. Kamado, Y. Kojima, *Scr. Mater.* 61 (2009) 636–639, doi:[10.1016/j.scriptamat.2009.05.044](https://doi.org/10.1016/j.scriptamat.2009.05.044).
- [47] Z. Luo, S. Zhang, Y. Tang, D. Zhao, *J. Alloy. Compd.* 209 (1994) 275–278, doi:[10.1016/0925-8388\(94\)91113-4](https://doi.org/10.1016/0925-8388(94)91113-4).
- [48] Z.P. Luo, S.Q. Zhang, *J. Mater. Sci. Lett.* 19 (2000) 813–815, doi:[10.1023/A:1006793411506](https://doi.org/10.1023/A:1006793411506).
- [49] Y. Kawamura, K. Hayashi, A. Inoue, T. Masumoto, *Mater. Trans.* 42 (2001) 1172–1176, doi:[10.2320/matertrans.42.1172](https://doi.org/10.2320/matertrans.42.1172).
- [50] J.K. Kim, L. Jin, S. Sandlöbes, D. Raabe, *Sci. Rep.* 7 (2017) 1–8, doi:[10.1038/s41598-017-04343-y](https://doi.org/10.1038/s41598-017-04343-y).
- [51] D. Xu, E.H. Han, Y. Xu, *Prog. Nat. Sci. Mater. Int.* 26 (2016) 117–128, doi:[10.1016/j.pnsc.2016.03.006](https://doi.org/10.1016/j.pnsc.2016.03.006).
- [52] X.F. Gu, T. Furuhashi, L. Chen, P. Yang, *Acta Metall. Sin. (English Lett.)* 32 (2019) 187–193, doi:[10.1007/s40195-018-0840-3](https://doi.org/10.1007/s40195-018-0840-3).

- [53] E. Abe, Y. Kawamura, K. Hayashi, A. Inoue, *Acta Mater.* 50 (2002) 3845–3857, doi:10.1016/S1359-6454(02)00191-X.
- [54] T. Honma, T. Ohkubo, S. Kamado, K. Hono, *Acta Mater.* 55 (2007) 4137–4150, doi:10.1016/j.actamat.2007.02.036.
- [55] K. Kishida, K. Nagai, A. Matsumoto, A. Yasuhara, H. Inui, *Acta Mater.* 99 (2015) 228–239, doi:10.1016/j.actamat.2015.08.004.
- [56] P. Mao, Y. Xin, K. Han, Z. Liu, Z. Yang, *Mater. Sci. Eng. A* 777 (2020) 139019, doi:10.1016/j.msea.2020.139019.
- [57] Y. Kawamura, M. Yamasaki, *Mater. Trans.* 48 (2007) 2986–2992, doi:10.2320/matertrans.MER2007142.
- [58] K. Xu, S. Liu, K. Chang, Y. Liang, Y. Du, Z. Jin, *J. Magnes. Alloy.* 9 (2021) 144–155, doi:10.1016/j.jma.2019.12.008.
- [59] Y. Ruan, C. Li, Y. Ren, X. Wu, R. Schmid-Fetzer, C. Guo, Z. Du, *J. Mater. Sci. Technol.* 68 (2021) 147–159, doi:10.1016/j.jmst.2020.08.019.
- [60] S.R. Agnew, *Advances in wrought magnesium alloys: fundamentals of processing, properties and applications* (2012) 63–104, doi:10.1016/B978-1-84569-968-0.50002-8.
- [61] M.R. Barnett, *Mater. Sci. Eng. A* 464 (2007) 1–7, doi:10.1016/j.msea.2006.12.037.
- [62] J. Shao, Z. Chen, T. Chen, Z. Hu, X. Zhou, C. Liu, *J. Magnes. Alloy.* 4 (2016) 83–88, doi:10.1016/j.jma.2016.03.001.
- [63] X.H. Shao, Z.Q. Yang, X.L. Ma, *Philos. Mag. Lett.* 94 (2014) 150–156, doi:10.1080/09500839.2014.885123.
- [64] M. Matsuda, S. Ii, Y. Kawamura, Y. Ikuhara, M. Nishida, *Mater. Sci. Eng. A* 386 (2004) 447–452, doi:10.1016/j.msea.2004.08.006.
- [65] J.K. Kim, S. Sandlöbes, D. Raabe, *Acta Mater.* 82 (2015) 414–423, doi:10.1016/j.actamat.2014.09.036.
- [66] J.B. Hess, C.S. Barrett, *Trans. Am. Inst. Min. Metall. Pet. Eng.* 185 (1949) 599–606, doi:10.2214/AJR.09.3938.
- [67] M.W. Barsoum, T. Zhen, S.R. Kalidindi, M. Radovic, A. Murugaiyah, *Nat. Mater.* 2 (2003) 107–111, doi:10.1038/nmat814.
- [68] H. Liu, H. Huang, C. Wang, J. Sun, J. Bai, F. Xue, A. Ma, X.B. Chen, *JOM* 71 (2019) 3314–3327, doi:10.1007/s11837-019-03610-9.
- [69] R. Lu, J. Wang, Y. Chen, D. Qin, W. Yang, Z. Wu, *J. Alloy. Compd.* 639 (2015) 541–546, doi:10.1016/j.jallcom.2015.03.208.
- [70] M. Yamasaki, T. Anan, S. Yoshimoto, Y. Kawamura, *Scr. Mater.* 53 (2005) 799–803, doi:10.1016/j.scriptamat.2005.06.006.
- [71] M. Yamasaki, M. Sasaki, M. Nishijima, K. Hiraga, Y. Kawamura, *Acta Mater.* 55 (2007) 6798–6805, doi:10.1016/j.actamat.2007.08.033.
- [72] H. Liu, H. Huang, J.P. Sun, C. Wang, J. Bai, A. Bin Ma, X.H. Chen, *Acta Metall. Sin.* 32 (2019) 269–285 English Lett., doi:10.1007/s40195-018-0862-x.
- [73] L.T. Yuan, G. IL Bi, Y.D. Li, J. Jiang, Y. xXang Han, D.Q. Fang, Y. Ma, *Trans. Nonferr. Met. Soc. China* 27 (2017) 2381–2389 English Ed., doi:10.1016/S1003-6326(17)60264-4.
- [74] P. Cheng, Y. Zhao, R. Lu, H. Hou, *J. Alloy. Compd.* 764 (2018) 226–238, doi:10.1016/j.jallcom.2018.06.056.
- [75] K. Wang, J. Wang, S. Huang, S. Gao, S. Guo, S. Liu, X. Chen, F. Pan, *Mater. Sci. Eng. A* 733 (2018) 267–275, doi:10.1016/j.msea.2018.07.050.
- [76] Z. Ding, Y. Zhao, R. Lu, H. Pei, H. Hou, *J. Mater. Res.* 33 (2018) 1797–1805, doi:10.1557/jmr.2018.100.
- [77] X. Zhou, Y. Yao, J. Zhang, X. Lu, K. Xu, H. Liu, Z. Wu, *Mater. Sci. Eng. A* (2020) 794, doi:10.1016/j.msea.2020.139934.
- [78] H. Liao, J. Kim, T. Lee, J. Song, J. Peng, B. Jiang, F. Pan, *J. Magnes. Alloy.* 8 (2020) 1120–1127, doi:10.1016/j.jma.2020.06.009.
- [79] D.A. Porter, K.E. Easterling, M.Y. Sherif, *Phase transformation in metals and alloys, 3rd ed., CRC Press, 2009.*
- [80] T. Li, D.J. Chen, W. Liu, J.W. Yuan, J. Qu, *IOP Conf. Ser. Mater. Sci. Eng.* (2019) 542, doi:10.1088/1757-899X/542/1/012040.
- [81] J. Zhang, M. Xu, X. Teng, M. Zuo, *J. Magnes. Alloy.* 4 (2016) 319–325, doi:10.1016/j.jma.2016.09.003.
- [82] Y. Liu, G. Yuan, S. Zhang, X. Zhang, C. Lu, W. Ding, *Mater. Trans.* 49 (2008) 941–944, doi:10.2320/matertrans.mc200767.
- [83] D.K. Xu, W.N. Tang, L. Liu, Y.B. Xu, E.H. Han, J. Alloy. Compd. 461 (2008) 248–252, doi:10.1016/j.jallcom.2007.07.096.
- [84] J. Gröbner, A. Kozlov, X.Y. Fang, S. Zhu, J.F. Nie, M.A. Gibson, R. Schmid-Fetzer, *Acta Mater.* 90 (2015) 400–416, doi:10.1016/j.actamat.2015.02.044.
- [85] M. Qian, D.H. StJohn, M.T. Frost, *Scr. Mater.* 50 (2004) 1115–1119, doi:10.1016/j.scriptamat.2004.01.026.
- [86] M. Qian, A. Das, *Scr. Mater.* 54 (2006) 881–886, doi:10.1016/j.scriptamat.2005.11.002.
- [87] W. Zhang, Z. Feng, X. Li, Y. Chen, *Mater. Res.* 23 (2020) 1–8, doi:10.1590/1980-5373-MR-2019-0539.
- [88] Y. Wang, W. Rong, Y.J. Wu, L.M. Peng, J. Chen, W.J. Ding, *J. Alloy. Compd.* 698 (2017) 1066–1076, doi:10.1016/j.jallcom.2016.12.165.
- [89] J. Yuan, T. Li, K. Zhang, X. Li, Y. Li, M. Ma, G. Shi, Z. Du, W. Liu, Y. Peng, *Materials (Basel)* 14 (2021) 1–10.
- [90] X. Zhang, L. Meng, C. Fang, P. Peng, F. Ja, H. Hao, *Mater. Sci. Eng. A* 586 (2013) 19–24, doi:10.1016/j.msea.2013.05.089.
- [91] Z. Yu, C. Xu, J. Meng, X. Zhang, S. Kamado, *Mater. Sci. Eng. A* 713 (2018) 234–243, doi:10.1016/j.msea.2017.12.070.
- [92] L. Hong, R. Wang, X. Zhang, *J. Mater. Eng. Perform.* 30 (2021) 6000–6008, doi:10.1007/s11665-021-05782-5.
- [93] S. Wu, J. Zhang, C. Xu, K. Nie, X. Niu, Z. You, *China Foundry* 14 (2017) 34–38, doi:10.1007/s41230-017-5074-x.
- [94] Z.P. Luo, H. Hashimoto, *Micron* 31 (2000) 487–492, doi:10.1016/S0968-4328(99)00128-6.
- [95] H.S. Jiang, X.G. Qiao, C. Xu, M.Y. Zheng, K. Wu, S. Kamado, *Mater. Des.* 108 (2016) 391–399, doi:10.1016/j.matdes.2016.06.116.
- [96] V.E. Bazhenov, S.S. Saidov, Y.V. Tselovalnik, O.O. Voropaeva, I.V. Plisetskaya, A.A. Tokar, A.I. Bazlov, V.A. Bautin, A.A. Komissarov, A.V. Kolygin, V.D. Belov, *Trans. Nonferr. Met. Soc. China* 31 (2021) 1276–1290 English Ed., doi:10.1016/S1003-6326(21)65577-2.
- [97] K. Yamada, Y. Okubo, M. Shiono, H. Watanabe, S. Kamado, Y. Kojima, *Mater. Trans.* 47 (2006) 1066–1070, doi:10.2320/matertrans.47.1066.
- [98] X. Zeng, Y. Wu, L. Peng, D. Lin, W. Ding, Y. Peng, *Acta Metall. Sin.* 46 (2010) 1041–1046, doi:10.3724/SP.J.1037.2009.00833.
- [99] W. Liu, Z.W. Du, T. Li, K. Zhang, X.L. Han, Y.G. Peng, J. Zhang, J.W. Yuan, S.F. Liu, Z. Pang, *Trans. Nonferr. Met. Soc. China* 29 (2019) 2047–2055 English Ed., doi:10.1016/S1003-6326(19)65111-3.
- [100] Z. Tian, Q. Yang, K. Guan, Z.Y. Cao, J. Meng, *Rare Met.* 40 (2021) 2188–2196, doi:10.1007/s12598-020-01510-5.
- [101] Z. Yu, X. Xu, B. Du, K. Shi, K. Liu, S. Li, X. Han, T. Xiao, W. Du, *Acta Metall. Sin.* (2021) English Lett., doi:10.1007/s40195-021-01269-3.
- [102] J. Zheng, B. Chen, *Mater. Lett.* 176 (2016) 223–227, doi:10.1016/j.matlet.2016.04.114.
- [103] L. Zhou, J. Zheng, X. Wang, X. Zeng, B. Chen, *J. Mater. Res.* 35 (2020) 172–184, doi:10.1557/jmr.2019.406.
- [104] Q. Zhang, W. Liu, G. Wu, L. Zhang, W. Ding, *Acta Metall. Sin.* 33 (2020) 1505–1517 English Lett., doi:10.1007/s40195-020-01106-z.
- [105] C. Huang, C. Liu, S. Jiang, Y. Wan, *J. Alloy. Compd.* 874 (2021) 159825, doi:10.1016/j.jallcom.2021.159825.
- [106] L. Yu, X. Chen, S. Wang, B. Chen, *J. Mater. Res.* 34 (2019) 3545–3553, doi:10.1557/jmr.2019.147.
- [107] K. Wen, W.B. Du, K. Liu, Z.H. Wang, S.B. Li, *Rare Met.* 35 (2016) 443–449, doi:10.1007/s12598-016-0735-2.
- [108] J. Li, Z. He, P. Fu, Y. Wu, L. Peng, W. Ding, *Mater. Sci. Eng. A* 651 (2016) 745–752, doi:10.1016/j.msea.2015.11.021.
- [109] S. Zhang, W. Liu, X. Gu, C. Lu, G. Yuan, W. Ding, *J. Alloy. Compd.* 557 (2013) 91–97, doi:10.1016/j.jallcom.2012.12.093.
- [110] W. Fu, R.H. Wang, H. Xue, J. Kuang, J.Y. Zhang, G. Liu, J. Sun, *J. Alloy. Compd.* 747 (2018) 197–210, doi:10.1016/j.jallcom.2018.02.328.
- [111] W. Rong, Y. Wu, Y. Zhang, M. Sun, J. Chen, L. Peng, W. Ding, *Mater. Charact.* 126 (2017) 1–9, doi:10.1016/j.matchar.2017.02.010.
- [112] M.M. Avedesian, H. Baker, *ASM specialty handbook, Magnesium and magnesium alloys, ASM International, Materials Park, OH, 1999 Materials Park, OH.*